An ALMA Study of the FU Ori-type Object V900 Mon

Implications for the Progenitor

Takami, M.; Chen, T.-S.; Liu, H.B.; Hirano, N.; Kóspál, Á.; Ábrahám, P.; Vorobyov, E.I.; Cruz-Sáenz de Miera, F.; Csengeri, T.; Green, J.; Hogerheijde, M.; Hsieh, T.H.; Karr, J.L.; Dong, R.; Trejo, A.; Chen, L.

DOI
10.3847/1538-4357/ab43c8

Publication date
2019

Document Version
Final published version

Published in
Astrophysical Journal

The Astrophysical Journal, 884:146 (16pp), 2019 October 20 https://doi.org/10.3847/1538-4357/ab43c8

An ALMA Study of the FU Ori–type Object V900 Mon: Implications for the Progenitor

Michihiro Takami[1], Tsu-Sheng Chen[1], Hauyu Baobab Liu[1], Naomi Hirano[1], Ágnes Kóspál[2,3], Péter Ábrahám[2], Eduard I. Vorobyov[4,5], Fernando Cruz-Sáenz de Miera[2], Timea Csengeri[6], Joel Green[7], Michiel Hogerheijde[8], Tien-Hao Hsieh[1], Jennifer L. Karr[1], Ruobing Dong[1,9], Alfonso Trejo[1], and Lei Chen[2]

[1] Institute of Astronomy and Astrophysics, Academia Sinica, 11F of Astronomy-Mathematics Building, AS/NTU No.1, Sec. 4, Roosevelt Rd., Taipei 10617, Taiwan, R.O.C.; hiro@asiaa.sinica.edu.tw

[2] Konkoly Observatory, Research Centre for Astronomy and Earth Sciences, Hungarian Academy of Sciences, Konkoly-Thege Miklós út 15-17, 1121 Budapest, Hungary

[3] Max Planck Institute for Astronomy, Königstuhl 17, D-69117 Heidelberg, Germany

[4] Research Institute of Physics, Southern Federal University, Roston-on-Don 344090, Russia

[5] Department of Astrophysics, University of Vienna, Vienna A-1080, Austria

[6] Max-Planck-Institut für Radioastronomie, Auf dem Hügel 69, D-53121 Bonn, Germany

[7] Space Telescope Science Institute, 3700 San Martin Dr., Baltimore, MD 21218, USA

[8] Leiden Observatory, Leiden University & Anton Pannekoek Institute for Astronomy, University of Amsterdam, P.O. Box 9513, 2300 RA, Leiden, The Netherlands

[9] Department of Physics & Astronomy, University of Victoria, Victoria, BC, V8P 1A1, Canada

Received 2019 July 10; revised 2019 September 5; accepted 2019 September 10; published 2019 October 21

Abstract

We present ALMA observations of ^{12}CO, ^{13}CO, and C^{18}O $J = 2$–1 lines and the 230 GHz continuum for the FU Ori–type object (FUor) V900 Mon ($d \sim 1.5$ kpc), for which the accretion burst was triggered between 1953 and 2009. We identified CO emission associated with a molecular bipolar outflow extending up to an $\sim 10^4$ au scale and a rotating molecular envelope extending over $>10^4$ au. The interaction with the hot energetic FUor wind, which was observed using optical spectroscopy, appears limited to a region within ~400 au of the star. The envelope mass and collimation of the extended CO outflow suggest that the progenitor of this FUor is a low-mass Class I young stellar object (YSO). These parameters for V900 Mon, another FUor, and a few FUor-like stars are consistent with the idea that FUor outbursts are associated with normal YSOs. The continuum emission is marginally resolved in our observations with a $0\farcs2 \times 0\farcs15$ ($\sim 300 \times 225$ au) beam, and a Gaussian model provides a deconvolved FWHM of ~90 au. The emission is presumably associated with a dusty circumstellar disk, plus a possible contribution from a wind or wind cavity close to the star. The warm compact nature of the disk continuum emission could be explained with viscous heating of the disk, while gravitational fragmentation in the outer disk and/or a combination of grain growth and their inward drift may also contribute to its compact nature.

Unified Astronomy Thesaurus concepts: Stellar accretion disks (1579); Circumstellar envelopes (237); Stellar jets (1607); Stellar winds (1636); FU Orionis stars (553); Circumstellar disks (235)

1. Introduction

Most of the stars in our Galaxy have masses below a few solar masses. We do not understand the physical mechanism by which these stars ("low-mass" stars) accrete their masses well.

The evolution of low-mass young stellar objects (YSOs) is characterized and classified using their infrared (IR) spectral energy distribution (SED; Class 0→ I→II→III; Stahler & Palla 2005). Muzerolle et al. (1998) measured the mass accretion rates for a sample of Class I–II YSOs using the Br γ line and showed that steady mass accretion can explain only a fraction of their final stellar masses. This issue is also corroborated by the facts below. At the pre-main-sequence phase of their evolution ("Class II–III"), in which the circumstellar gas+dust envelope has already been dissipated, the masses of the associated circumstellar disks are significantly smaller than the stars (e.g., Williams & Cieza 2011), indicating that the stellar masses have been developed primarily during the Class 0–I phases. It has been suggested that their protostellar luminosities tend to be significantly lower than theoretical predictions for steady mass accretion, e.g., by a factor of 10–10^3 (the "luminosity problem"; see, e.g., Kenyon et al. 1990; Audard et al. 2014; Dunham et al. 2014).

A key phenomenon that may solve the above issues is episodic mass accretion, observed in some YSOs as a sudden increase of flux at optical and near-IR wavelengths. The above trends are explained if Class 0–I YSOs are associated with accretion outbursts whose periods are significantly shorter than the timescale of these evolutionary phases (and therefore with a small chance of observation) but that are responsible for a significant fraction of the final stellar masses (e.g., Kenyon et al. 1990; Muzerolle et al. 1998; Calvet et al. 2000).

The FU Orionis objects (hereafter FUors) are a class of YSOs that undergo the most active and violent accretion outbursts, during which the accretion rate rapidly increases by a factor of 100–1000 and remains high for several decades or more. Such outbursts have been observed toward about 10 stars to date. Another dozen YSOs exhibit optical or near-IR spectra similar to FUors, distinct from many other YSOs, but outbursts have never been observed. Their spectra suggest disk accretion with high accretion rates similar to FUors. These are classified as FUor candidates or FUor-like objects. See Audard et al. (2014) for a review for FUors and FUor-like objects. Their optical and near-IR spectra indicate that the optical and near-IR emission from these objects is dominated by a warm disk photosphere (see Hartmann & Kenyon 1996; Audard et al. 2014, for reviews). This is in contrast to many other normal Class I–II YSOs, whose optical and near-IR emission is dominated by the star and featureless dust continuum (e.g., Greene & Lada 1996; Doppmann et al. 2005; Connelley & Greene 2010). A sudden increase in the accretion rate heats up the inner disk ($r < 1$ au) of the FUors, observable as continuum emission at optical and IR wavelengths.

The triggering mechanism of FUor outbursts is not clear, despite numerous observations at a variety of wavelengths, theoretical work, and numerical simulations. The proposed mechanisms include (1) gravitational/thermal/magnetorotational instabilities in the disk and (2) the perturbation of the disk by an external body (see Audard et al. 2014, for a review). Liu et al. (2016) and Takami et al. (2018) revealed a variety of distributions in the near-IR scattered light that can be attributed to gravitationally unstable disks and trails of clump ejections in such disks. These results support gravitational instabilities in disks as a triggering mechanism of the outbursts, as demonstrated with some hydrodynamical simulations (e.g., Vorobyov & Basu 2015; Dong et al. 2016; Zhao et al. 2018). Dunham & Vorobyov (2012) carried out radiative transfer calculations for a number of hydrodynamical simulations with gravitationally unstable disks and demonstrated that this physical mechanism can also solve the "luminosity problem" described above. According to their simulations, accretion bursts contribute to only up to 35% of the final stellar mass, in contrast to the previous arguments that FUor outbursts are essential for low-mass protostellar evolution (e.g., Muzerolle et al. 1998; Calvet et al. 2000).

However, another key question still remains: are FUor outbursts associated with most low-mass YSOs? In other words, are FUors peculiar YSOs, or is this a specific phase for the evolution of most low-mass YSOs? As with normal YSOs, many of these observations show extended molecular outflows, envelopes, and disks associated with FUors and FUor-like objects. The IR-to-millimeter emission and mid-IR silicate absorption indicate that FUors are associated with an envelope similar to those of Class 0–I YSOs (e.g., Sandell & Weintraub 2001; Green et al. 2006, 2013; Quanz et al. 2007; Gramajo et al. 2014; Fehér et al. 2017; Kóspál et al. 2017b). Mid-IR spectroscopy shows that some FUors are associated with silicate absorption like Class I YSOs, while other objects are associated with emission like Class II YSOs (Green et al. 2006; Quanz et al. 2007). Quanz et al. (2007) attributed this trend to an evolution of the FUors similar to the Class 0–I to Class II transitions of normal YSOs.

Thanks to a combination of high angular resolution and sensitivity, the Atacama Large Millimeter/submillimeter Array (ALMA) has recently begun to provide detailed information about their cold ($\ll$100 K) extended molecular outflows, envelopes, and disks, which is potentially powerful for further investigating whether FUor outbursts occur in most low-mass YSOs. The FUors and FUor-like objects observed using ALMA include FU Ori (FUor; Hales et al. 2015), V883 Ori (FUor-like; Cieza et al. 2016; Ruíz-Rodríguez et al. 2017a), V346 Nor (FUor; Kóspál et al. 2017b), V2775 Ori (FUor-like; Zurlo et al. 2017), HBC 494 (FUor-like; Ruíz-Rodríguez et al. 2017b), and L1551 IRS 5 (FUor-like; Cruz-Sáenz de Miera et al. 2019).

In this paper, we present ALMA observations of the 230 GHz ($\lambda = 1.3$ mm) continuum and ^{12}CO, ^{13}CO, and C^{18}O $J = 2$–1 lines for the FUor V900 Mon (2MASS 06572222–0823176). This object underwent a major increase in brightness between 1953 and 2009, by at least 4 mag in the optical (Thommes et al. 2011; Reipurth et al. 2012), and it may still be brightening (Varricatt et al. 2015). The luminosity ($\sim$200 $L_\odot$[10]) and the optical and near-IR spectra observed during the outburst are similar to those of FUors (Reipurth et al. 2012; Connelley & Reipurth 2018). The star has a much higher reddening ($A_V \sim 13$ mag) than many other FUors ($<$5 for many cases) but is comparable to FUor-like objects ($A_V = 2$–40 mag; Audard et al. 2014). While the IR SED suggests the presence of an envelope (Reipurth et al. 2012; Gramajo et al. 2014), its mass may be modest. Kóspál et al. (2017b) conducted single-dish observations of ^{12}CO $J = 3$–2, ^{12}CO $J = 4$–3, and ^{13}CO $J = 3$–2 with a 15″–19″ resolution. Unlike several other FUors, these authors did not detect these CO emissions at the stellar position, providing an upper mass limit for the envelope of 0.1 $M_\odot$. This fact is corroborated by a mass estimate using a detailed model of the SED by Gramajo et al. (2014). The envelope mass derived by these authors is 0.027 $M_\odot$, one of the lowest among the 23 FUors and FUor-like objects in their study (0–1.5 $M_\odot$).

Using ALMA, we were able to detect emission associated with a molecular bipolar outflow, rotating molecular envelope, and probable disk associated with V900 Mon. The rest of the paper is organized as follows. In Section 2 we describe the observations. In Section 3 we show various images for continuum and CO emission and CO line profiles for selected regions. In Section 4 we discuss the molecular bipolar outflow, envelope, disk, and interaction with a hot ($\gg$1000 K) energetic FUor wind[11] observed in optical spectra toward the star. In Section 5 we discuss whether FUor outbursts are associated with normal YSOs. In Section 6 we give our conclusions. Throughout the paper, we adopt a distance of 1.5 kpc ($1.5^{+0.3}_{-0.2}$ kpc including the uncertainty; Gaia Collaboration et al. 2018).

2. Observations and Data Reduction

We observed V900 Mon with the ALMA 12 m array on 2017 April 20 and July 27 and the ACA on 2016 October 11 (project code: 2016.1.00209.S; PI: Michihiro Takami). The pointing and phase referencing center is R.A. (J2000) = 06:57:22.224, decl. (J2000) = −08:23:17.64. The spectral setup of all of our observations is identical. There were two 1.875 GHz wide spectral windows (1.3 km s^{-1} velocity resolution) centered at 216.9 and 232.2 GHz, two 58.6 MHz wide spectral windows to cover ^{13}CO $J = 2$–1 and C^{18}O $J = 2$–1 at a 0.083 km s^{-1} velocity resolution, and one 58.6 MHz wide spectral window to cover ^{12}CO $J = 2$–1 at a 0.040 km s^{-1} velocity resolution. These spectral windows tracked the systemic velocity $V_{\rm LSR} \sim 13.5$ km s^{-1}.

These observations covered *uv* distance ranges of 20–3500 and 9.3–46 m, respectively. These configurations provided a largest recoverable scale of 29″. Other details of the observations are summarized in Table 1.

The data were manually calibrated and phase self-calibrated using the CASA software package (McMullin et al. 2007) version 5.4. The self-calibration increased the signal-to-noise ratio only marginally. We fitted the continuum baselines using the CASA task `uvcontsub` and then jointly imaged all continuum data using the CASA task `tclean`. Table 2 summarizes the frequencies and beams of the continuum and

[10] Reipurth et al. (2012) measured 106 $L_\odot$, adopting a distance of 1.1 kpc. We scale this luminosity to the recent measurement of the distance based on *Gaia* DR2 ($1.5^{+0.3}_{-0.2}$ kpc).

[11] In this paper, we use the words "outflow" and "wind" following the literature in this research field. Throughout, an "outflow" in the paper implies extended ($\gg$100 au) molecular outflows primarily observed in millimeter CO emission. The presence of millimeter CO emission indicates a low temperature for the gas ($<$50 K). As described later, these outflows result from the interaction of a collimated jet or a wide-angled wind with the surrounding gas (e.g., Lee et al. 2002; Arce et al. 2007). The word "wind" is used for any other gas outflowing directly from the star or the inner disk, usually poorly collimated. (We use the word "jet" for a collimated flow.)

Table 1
Summary of the Observations

Epoch (No.)	Date UTC	Array	PWV (mm)	Flux/ Passband Calibrators[b]	Passband/ Gain Calibrator[b]	Gain Calibrator Flux[b] (Jy)	Time on Source (minutes)
1	2016 Oct 11	ACA	…[a]	J0522–3627/J0854+2006	J0725–0054	4.3/1.9	4.4
2	2017 Apr 20	ALMA	**2.7**	J0656–0323/J0510+1800	J0656–0323	2.3/0.56	3.0
3	2017 Jul 27	ALMA	**0.5**	J0522–3627/J0510+1800	J0654–0544	1.1/0.85	9.1

Notes. Values in bold indicate precipitable water vapor.
[a] Not recorded.
[b] Measured at 224 GHz.

Table 2
Frequencies and Angular Resolutions

Data	Frequency	Beam		Uncertainty[a]		Convolution				
						Convolution FWHM		Final Resolution	Uncertainty[a]	
	(GHz)	Size	P.A.	(K)	(mJy beam^{-1})	(pixel)	(arcsec)		(K)	(mJy beam^{-1})
Continuum	224.5416	0.″20 × 0.″15	−72.°3	0.037	**0.055**	…	…	…	…	…
^{12}CO $J = 2$–1	230.5380	0.″19 × 0.″14	−71.°3	**4.0**	**5.2**	5	0.″22	0.″29 × 0.″26	2.1	**7.8**
^{13}CO $J = 2$–1	220.3987	0.″19 × 0.″14	−71.°3	**4.1**	**4.9**	8	0.″36	0.″41 × 0.″39	1.4	**10**
C^{18}O $J = 2$–1	219.5604	0.″19 × 0.″14	−72.°4	**3.2**	**3.8**	11	0.″47	0.″51 × 0.″49	0.8	**9.3**

Note. Values in bold indicate uncertainties in intensity in units of Kelvin and mJy per beam. The middle columns are values before convolution, and the right columns are those after convolution.
[a] Excluding the absolute flux uncertainty of 10% for the ALMA Band 6 observations. The values for the lines are calculated for a 0.2 km s^{-1} channel.

CO lines. The Briggs Robust=0 weighted continuum image taken with ALMA achieved a 55 μJy beam^{-1} rms noise level.

The data cubes for the CO lines were made with spatial and velocity pixel sampling of 0.″02 and 0.2 km s^{-1}, respectively, and analyzed using Python (`numpy`, `scipy`, `matplotlib`). To increase the signal-to-noise ratio of the extended emission, we spatially convolved each velocity channel map using a two-dimensional Gaussian. In Table 2, we also summarize the parameters of the convolution and the final angular resolutions. The absence of the total power observations probably causes significant missing fluxes ($\gtrsim$20%) for these line observations.

3. Results

We present the continuum, the velocity channel maps of the CO lines in a wide field of view (FOV; 13″ × 13″), those close to the continuum source (a 4″ × 4″ FOV), and the line profiles in Sections 3.1–3.4, respectively.

3.1. Continuum

Figure 1 shows the 1.3 mm continuum image. The star is associated with a marginally resolved emission component with a 0.″2 × 0.″15 beam. We use the IMFIT routine within CASA to fit two-dimensional Gaussians to the continuum data and derive both continuum fluxes and disk sizes (deconvolved from the beam) for the resolved sources. As a result, we derive a flux of 9.0 ± 0.9 mJy and an FWHM for the emission region of (0.″067 ± 0.″008) × (0.″058 ± 0.″008) in the image plane. The latter corresponds to 100^{+35}_{-24} × 87^{+32}_{-22} au including the uncertainty in the distance.

The centroid position measured using Gaussian fitting is (α_{2000},δ_{2000}) = (06:57:22.221, −8:23:17.67), coinciding with the position of the Two Micron All Sky Survey (2MASS) point source within the accuracy of the 2MASS measurement (±0.″06). We do not find any other clear emission components within 19″ of the continuum source. The 3σ detection limits for the point source are 0.15 mJy at the source and 0.34 mJy at 15″ away from the source.

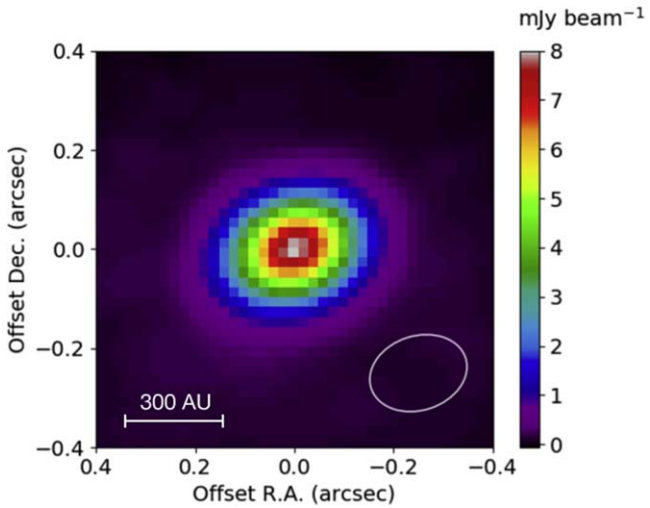

Figure 1. The 224.5 GHz continuum image of V900 Mon. The spatial offset is shown from the centroid position measured using Gaussian fitting (06:57:22.221−8:23:17.67). The white ellipse shows the beam size of the observations.

3.2. CO Emission in a Wide FOV (13″× 13″)

Figures 2 and 3 show the velocity channel maps of the ^{12}CO, ^{13}CO, and C^{18}O lines in a 13″ × 13″ FOV (i.e., up to ∼10,000 au scale from the continuum source). In Figure 2, we show the maps for the ^{12}CO and ^{13}CO lines, which have relatively high signal-to-noise, with a 0.2 km s^{-1} resolution. The signal-to-noise

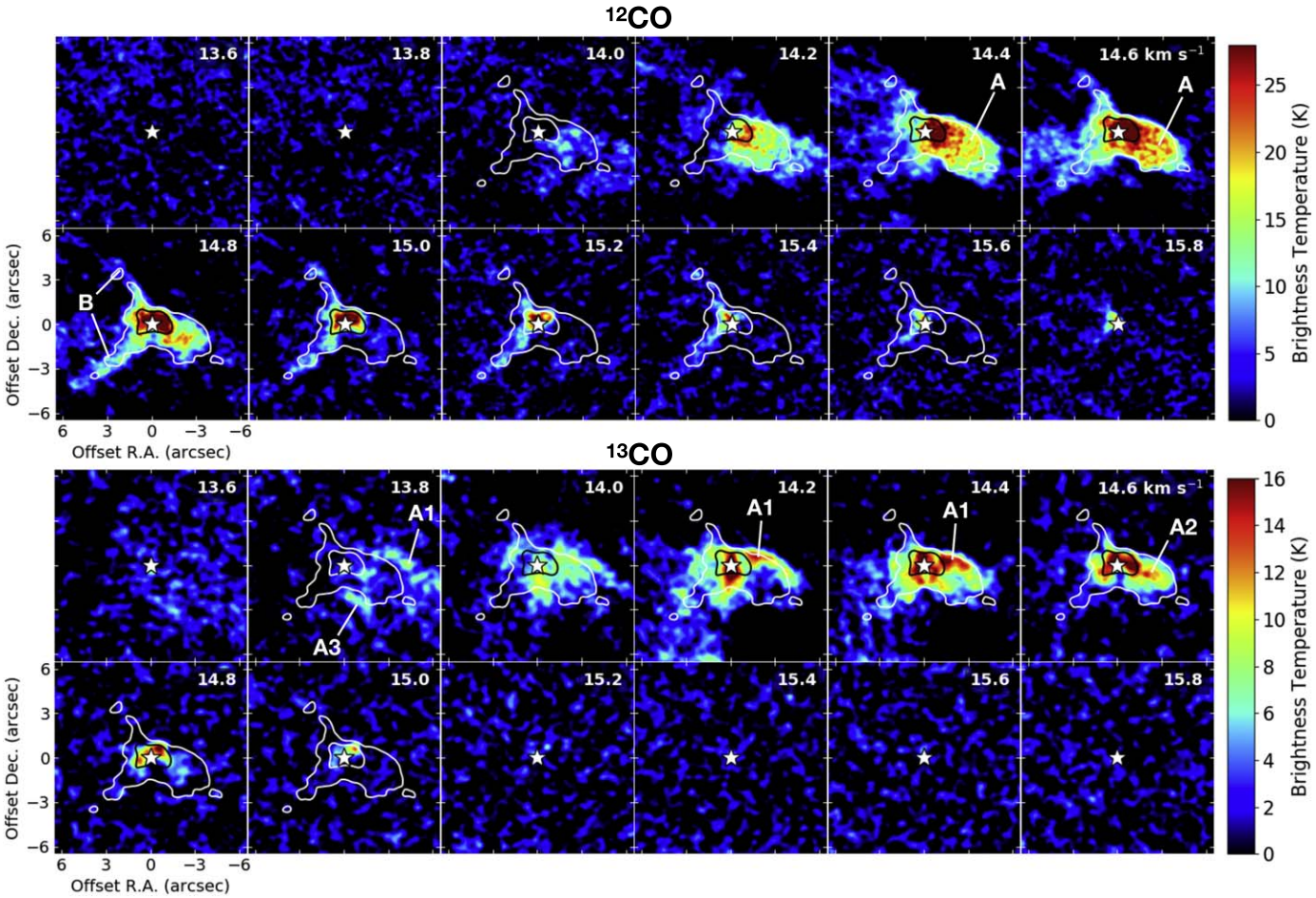

Figure 2. Velocity channel maps for the ^{12}CO and ^{13}CO lines, with a velocity resolution of 0.2 km s^{-1}. The velocity at the top right of each map is shown in the local standard rest frame. The (0″,0″) position, which is also shown in each map by a star, is the centroid position of the continuum (Section 3.1). A few arbitrary contours of the ^{12}CO moment-zero map (7.7 and 23.0 K km s^{-1}) are shown to clarify the different spatial distributions between different lines and velocities. The color of each contour (white/black) is arbitrarily chosen to highlight it against the color map. The features A, A1, A2, A3, and B discussed in the text are also marked.

ratio of the C^{18}O line is significantly lower; therefore, we show the velocity channel maps of this line in Figure 3 with a 0.4 km s^{-1} resolution. In Figure 3, we also show the maps for the ^{12}CO and ^{13}CO lines at the same velocities for comparison. Figure 4 shows the moment-zero maps of the three lines in the same FOV. For each figure, we show a few contours based on the moment-zero map of ^{12}CO to clarify the different emission distributions between different lines and velocities.

The ^{12}CO maps show the following prominent features: A is an oval feature that extends from the continuum position to the west at an ∼5″ (∼8000 au) scale at $v_{\rm LSR}$ = 14–15 km s^{-1}, and B is an arc to the east of the continuum position at $v_{\rm LSR}$ = 14.2–15.6 km s^{-1} at a 5″–7″ (∼7000–11,000 au) scale. As discussed later in Section 4.1 in detail, these are probably associated with blueshifted and redshifted molecular outflows, respectively.

Figure 2 shows that the blueshifted outflow A is also associated with ^{13}CO emission but observed only at the northern edge at 13.8–14.4 km s^{-1} (A1), the axis of the outflow at 14.6 km s^{-1} (A2), and the southern edge at 13.8 km s^{-1} (A3). These features are also seen in Figure 3 in the ^{13}CO emission at 13.7, 14.1, and 14.5 km s^{-1} and in the C^{18}O emission at 14.1 km s^{-1}. We see no ^{13}CO emission associated with the feature B.

In Figure 3, the C^{18}O emission shows diffuse extended emission in the north–south direction at 13.3, 13.7, and 14.1 km s^{-1} at an ∼5″ (∼8000 au) scale. The northern component (C) is seen at 13.3 and 13.7 km s^{-1}, while the southern component (D) is seen at 13.7 and 14.1 km s^{-1}. At 14.1 km s^{-1}, component D extends to the outside of the FOV of the figure, up to ∼10″ from the star. The C^{18}O emission does not show the A, A1, A2, A3, or B seen in the ^{12}CO and ^{13}CO emission, except the feature A1 at 14.1 km s^{-1}.

3.3. CO Emission Close to the Continuum Source (4″ × 4″ FOV)

In Figures 2–4, all of the lines show bright compact emission close to the continuum position. Figures 5 and 6 show the velocity channel maps for a 4″ × 4″ FOV, i.e., up to ∼3000 au scale from the continuum source. The figures show the ^{12}CO emission at $v_{\rm LSR}$ = 14.2–16.8 km s^{-1}, the ^{13}CO emission at 14.0–15.0 km s^{-1}, and the C^{18}O emission at 13.3–14.5 km s^{-1}. Bright ^{12}CO emission at 14.2–14.8 km s^{-1} is explained as the base of the blueshifted outflow A. The ^{12}CO emission is fainter at larger velocities, and its peak is offset to the north by up to ∼0.″5 at 14.8–15.2 km s^{-1}. The maps for 15.4–16.4 km s^{-1} show a compact component at the base of arc B, whose peak is marginally offset to the northeast by ∼0.″1 (hereafter B′).

In Figures 5 and 6, the ^{13}CO and C^{18}O emission shows kinematic structures significantly different from the ^{12}CO emission. In particular, the ^{13}CO emission in these figures

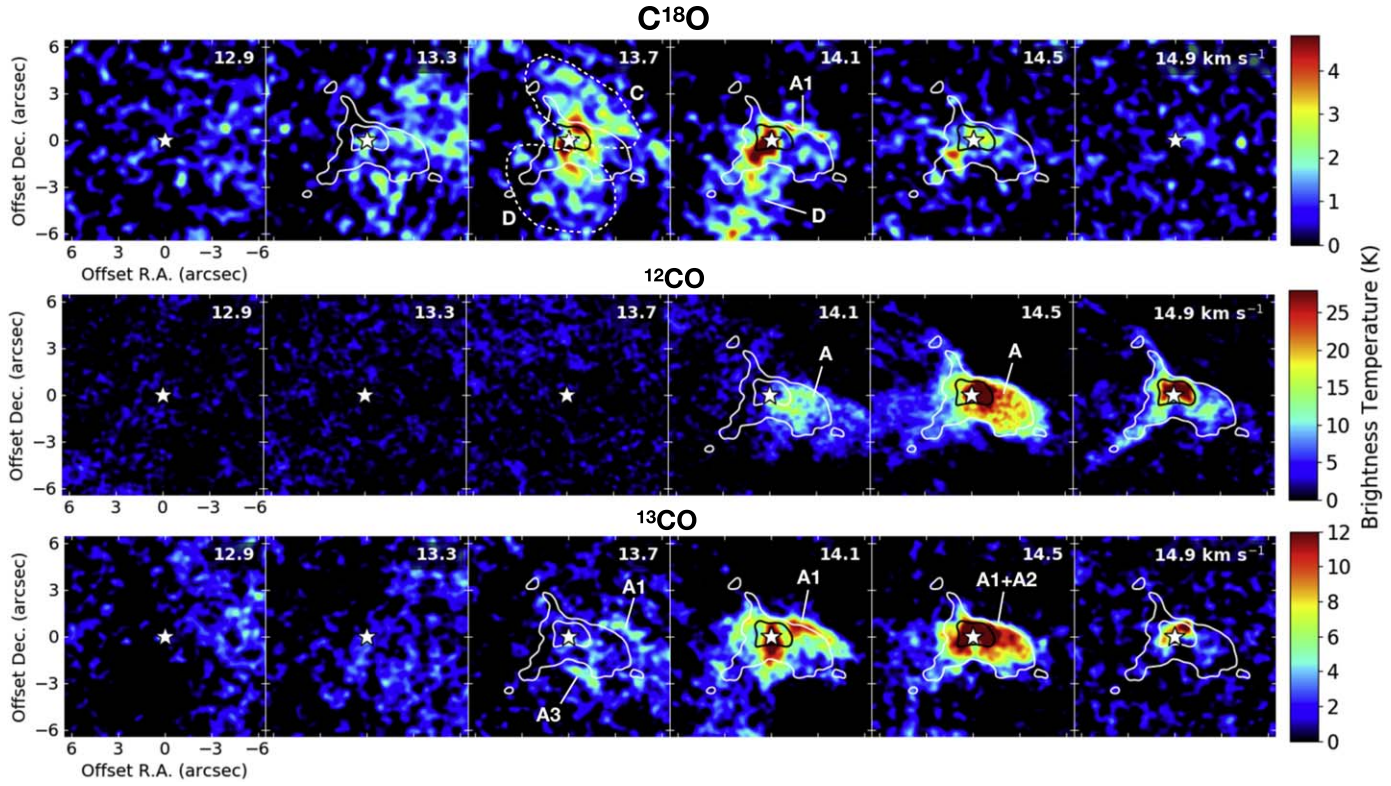

Figure 3. Same as Figure 2 but for the $C^{18}O$ (top), ^{12}CO (middle), and ^{13}CO lines (bottom) at 12.9–14.9 km s^{-1} (i.e., those we identify as the $C^{18}O$ emission) with a velocity resolution of 0.4 km s^{-1}. The features discussed in the text are also marked.

shows complicated intensity distributions at different velocities. The maps for 14.6 km s^{-1} in Figure 5 and 14.5 km s^{-1} in Figure 6 show bright extended emission to the west, which may correspond to the base of feature A2 shown in Figures 2 and 3. The maps for 14.2 km s^{-1} in Figure 5 and 14.1 km s^{-1} in Figure 6 show bright extended emission in the north–south direction. The $C^{18}O$ line at 13.7 and 14.1 km s^{-1} also shows extended emission in the north–south direction, which may be the base of emission components C and D in Figure 3. The brightest component (D′) is seen at 14.1 km s^{-1} in the southeast direction with a spatial scale up to 2″–3″, peaking at ∼0.″5 from the continuum position.

3.4. CO Line Profiles

Figure 7 shows the profiles of the three CO lines at the features discussed in Sections 3.2 and 3.3. The areas used for extracting the line profiles are shown in the bottom panels of Figure 4. We exclude A3 due to low signal-to-noise.

The ^{12}CO emission shows a relatively sharp cutoff of the flux at $V_{LSR} \sim 14$ km s^{-1}, and we observe zero or negative fluxes at smaller velocities. We attribute this to a combination of the following: (1) a contribution from extended emission associated with the parent cloud, which does not allow us to clearly observe emission associated with the YSO with large spatial frequencies, and (2) modest *uv* coverages of the observations. The ^{13}CO emission shows the same trend to some extent, but this line still shows weak fluxes at $V_{LSR} < 14$ km s^{-1}. In contrast, the $C^{18}O$ emission does not show this trend. Such differences are explained by different abundances of C and O isotopes ($^{12}C/^{13}C \sim 70$ and $^{16}O/^{18}O \sim 490$ for the local interstellar medium; Mathis 2000) and therefore different molecular abundances. In other words, a low abundance of $C^{18}O$ (and ^{13}CO) makes the extended emission associated with the molecular cloud significantly fainter, allowing the emission from the YSOs to be observed at these velocities. At $V_{LSR} > 14$ km s^{-1}, the ^{12}CO line profiles shown at B, B′, D, and D′ are associated with an excessive redshifted wing up to $V_{LSR} \sim 19$ km s^{-1}

We tabulate the peak and FWHM velocities for the $C^{18}O$ emission in Table 3. We do not know the systemic velocity of the target exactly; therefore, we describe the blueshift and redshift of the emission using "the reference velocity," which we tentatively define as 13.9 km s^{-1}. The peaks associated with features A and B are blueshifted and redshifted from the reference velocity by ∼0.3 km s^{-1}. Features A1 and A2, which are observed in A, show two peaks at the blueshifted and redshifted sides, respectively, with $\Delta v = 0.1$–0.7 km s^{-1} from the reference velocity. The blueshifted emission seems brighter than the redshifted emission for both profiles. The profiles for B', C, D, and D' show a single peak, offset from the reference velocity by 0.1–0.3, –(0.1–0.3), ∼0.3, and 0.1–0.3 km s^{-1}, respectively. The FWHM velocities measured at A, A1, A2, and B are 0.8–1.3 km s^{-1}, larger than those for C, D, and D' (0.5–0.8 km s^{-1}).

4. Extended Molecular Outflows, Envelope, Disk, and Hot Wind[12]

In Sections 4.1 and 4.2 we discuss CO emission associated with the extended molecular outflows and the envelope, respectively. In Section 4.3 we discuss the possible interaction of the hot FUor wind seen in optical spectra with the

[12] Please refer to the footnote in Section 1 for use of the words "outflow" and "wind."

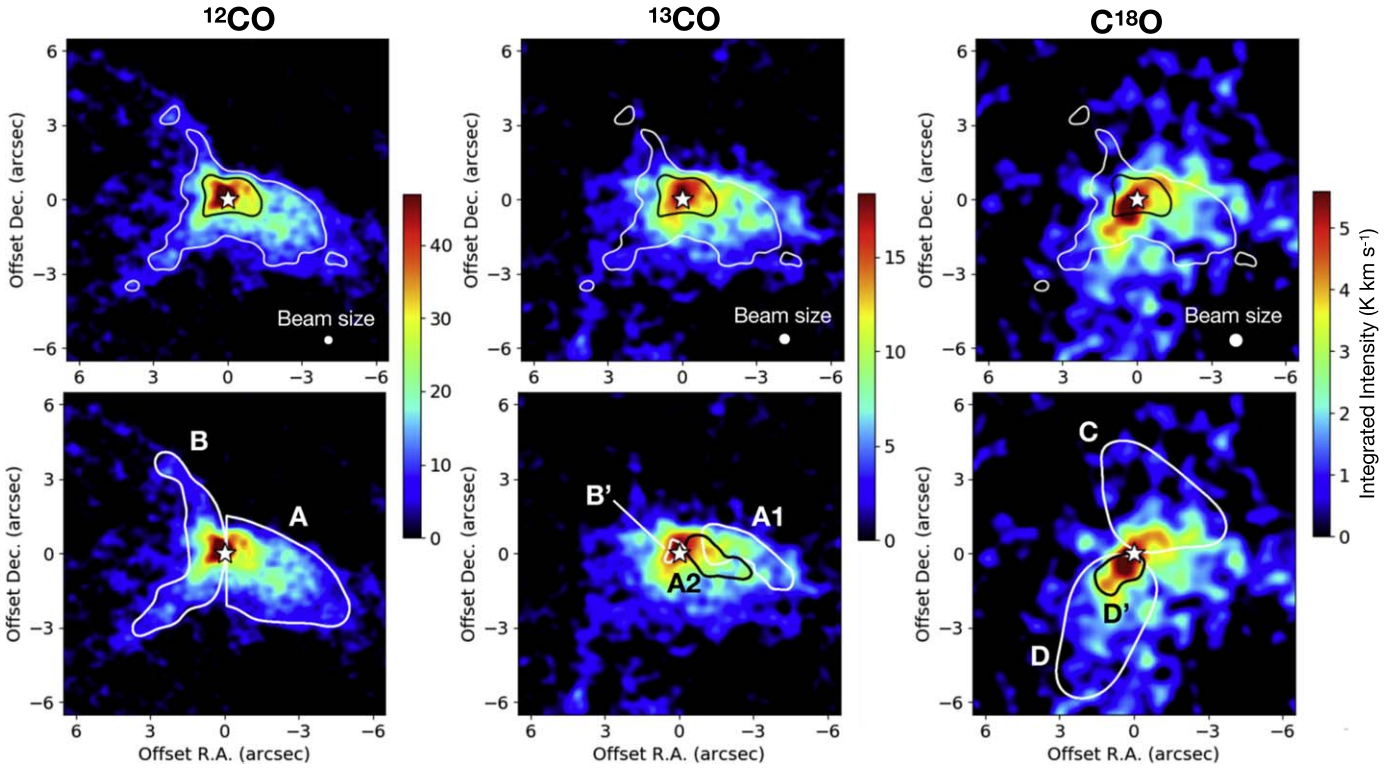

Figure 4. Moment-zero maps of the ^{12}CO, ^{13}CO, and C^{18}O lines. The color scale between the top and bottom panels is identical. In the top panels, we show the contours of the ^{12}CO emission as for Figures 2 and 3 to clarify the different spatial distributions between different lines. The bottom panels show the areas of the individual features (see the text and Figures 2, 3, 5, and 6) used for extracting the line profiles.

circumstellar environment. In Section 4.4 we discuss the compact nature of the continuum emission, which is primarily attributed to the circumstellar disk but with a possible contribution from an FUor wind or a wind cavity.

4.1. Extended Molecular Bipolar Outflow

The ^{12}CO, ^{13}CO, and C^{18}O channel maps show remarkably different intensity distributions even at the same velocities. Again, this is explained by the different optical thicknesses of these lines due to different molecular abundances. The ^{12}CO emission can be optically thick in general, and as a result, the observed fluxes highly depend on temperature distributions. In contrast, the optically thin C^{18}O emission is significantly affected by the column density distribution, as well as the temperature distribution.

Optical and near-IR imaging observations by Reipurth et al. (2012) showed the presence of a reflection nebula extending toward the southwest of the star at 20″–50″. In their near-IR image, the nebula extends to the west within 2″–3″ of the star, i.e., the same direction as feature A in ^{12}CO emission shown in Section 3.2. Reflection nebulae with similar morphologies are often associated with an outflow cavity in the protostellar envelope associated with many YSOs (e.g., Tamura et al. 1991; Lucas & Roche 1996, 1998; Padgett et al. 1999). The outflows associated with YSOs are usually bipolar (see, e.g., Arce et al. 2007, for a review), and the absence of the counterflow component at the optical and near-IR reflection nebulae is explained by a larger extinction toward the redshifted outflow.

Therefore, we conclude that features A and B in Figures 2–4 are associated with blueshifted and redshifted lobes of molecular outflows, respectively. Feature A does not show blueshifted ^{12}CO emission, presumably due to the parent molecular cloud (Section 3.4). Even so, the C^{18}O line profiles for A and B show blueshifts and redshifts (Figure 7 and Table 3), agreeing with this interpretation. The presence of the redshifted ^{12}CO emission in the blueshifted outflow lobe is explained (1) by the fact that the millimeter CO emission in molecular outflows results from interaction of a collimated jet or wide-angled wind with the surrounding gas (e.g., Lee et al. 2002; Arce et al. 2007) and (2) if the ^{12}CO emission in feature A is associated with the far side of the expanding outflow lobe.

The ^{13}CO line shows emission at the northern and southern edges of the blueshifted lobe of outflow A (A1 and A3 in Figures 2 and 3), suggesting the presence of gas compressed at the outflow cavity. Feature A2 in the ^{13}CO emission could be attributed to gas compression at the far side of the outflow cavity. The ^{13}CO emission at the northern edge of the blueshifted outflow (A1) is significantly brighter than that at the southern edge (A3), suggesting that the jet/wind interaction with the surrounding gas is not symmetric. The enhanced emission at the northern edge may be explained if the orientation of the jet/wind that drives the extended molecular outflow gradually moves counterclockwise, i.e., southwest in the past and west at present. This speculation is consistent with the fact that the reflection nebula in the outer region (>10″ of the star) is located in the southwest. Interestingly, we do not find such a brightness asymmetry between the northern and southern sides of counteroutflow B.

In contrast to some extended CO outflows, which show a fairly good symmetry between the blueshifted and redshifted outflow lobes with respect to the YSO (e.g., Arce & Sargent 2006), the blueshifted outflow lobe A is significantly brighter than the redshifted outflow lobe. This may be due to different densities of the ambient gas between the blueshifted

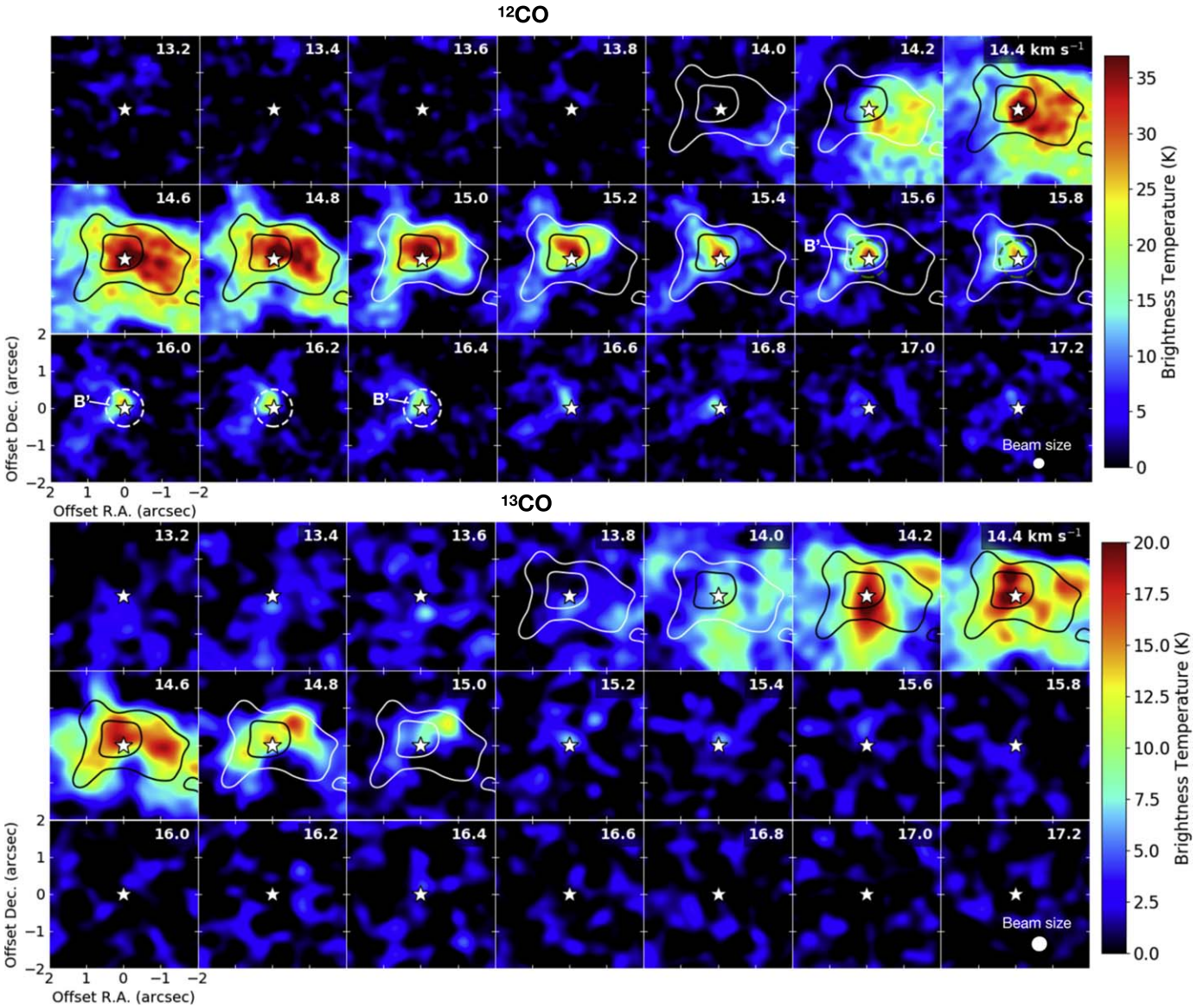

Figure 5. Same as Figure 2 but in a $4'' \times 4''$ FOV. The contour levels are 19 and 35 K km s^{-1} in the ^{12}CO emission. In some ^{12}CO maps, we draw a dashed circle centered on the continuum source, $0\farcs5$ in radius, to clarify the angular scale of the compact feature B′.

and redshifted sides, as with a blue-/redward asymmetry observed in some CO outflows (Lee et al. 2002). The single-dish observations of the molecular core by Kóspál et al. (2017b) show that the center of the core (and therefore the densest region) is located ∼30″ west from the target YSO. This fact would also explain the different opening angles of the blueshifted and redshifted lobes of the CO outflows, as more diffuse ambient gas requires less momentum to widen an outflow cavity, thereby making the opening angle of the redshifted lobe B wider.

4.2. Molecular Envelope

The diffuse C^{18}O emission components C, D, and D′ are presumably associated with a circumstellar envelope for the following reasons. These components are extended in the north–south direction, perpendicular to outflows A and B (Figures 2 and 4). The absence of these components in ^{12}CO and ^{13}CO indicates their relatively high column densities and low temperatures. Furthermore, these emission components also have FWHM velocities smaller than the outflow components (Section 3.4), exhibiting their relatively quiescent nature. All of these trends are what we expect for a circumstellar envelope associated with low-mass YSOs (e.g., Stahler & Palla 2005).

The northern and southern sides of the envelope (i.e., C and D, respectively) are blueshifted and redshifted, respectively (Section 3.4, Figure 7), indicative of its rotational motion. To further investigate this motion, we derive the line profiles at four apertures along the envelope emission, $1\farcs8$ and $5\farcs2$ from the star, and plot them in Figure 8. Their peak and FWHM velocities are tabulated in Table 3. The peak velocity at outer radii (N2 and S2) is ∼0.3 km s^{-1} offset from the reference velocity. This is comparable to that expected for Keplerian motion at the given distance (∼8000 au at $d = 1.5$ kpc) and assuming 1 $M_\odot$. In contrast, the peak offset velocity in the inner radii (0.1–0.3 km s^{-1}) is significantly lower than the Keplerian velocity (∼0.6 km s^{-1}) expected at the given distance (∼3000 au) and the same stellar mass. Therefore, the envelope gas up to

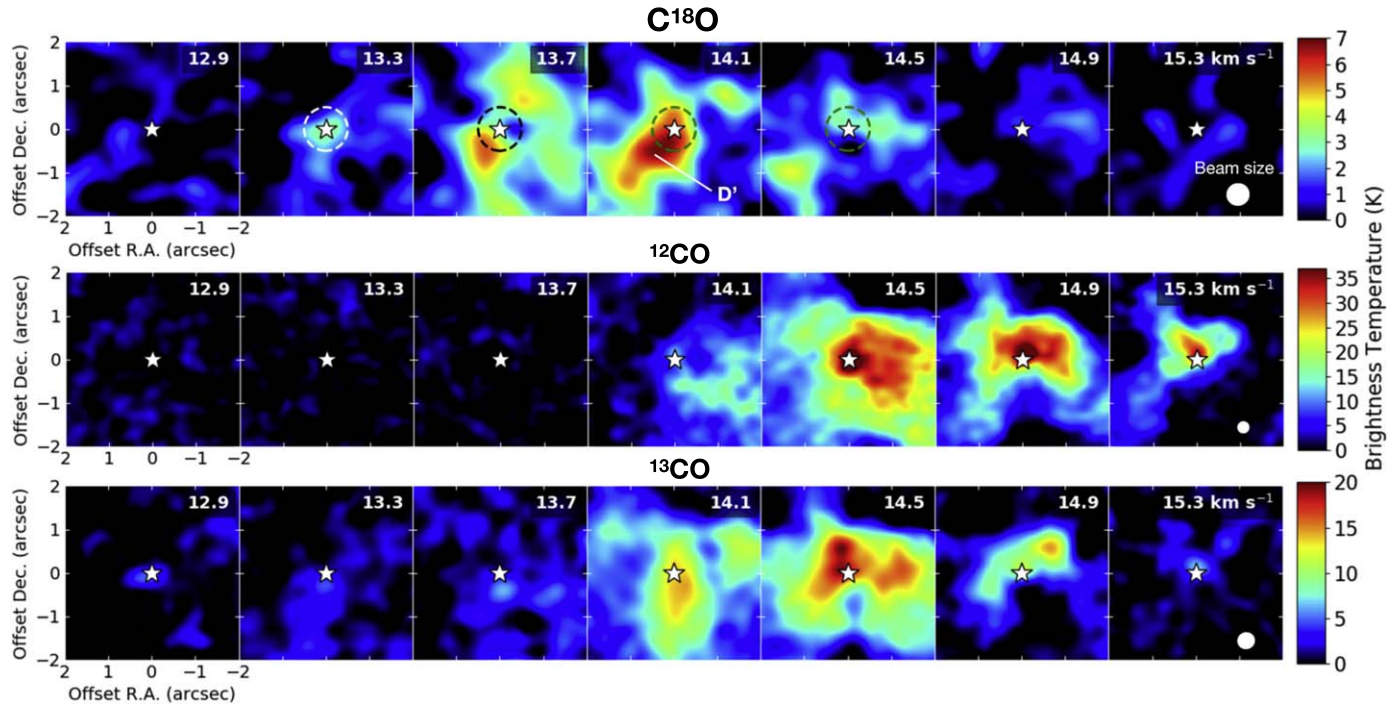

Figure 6. Same as Figure 3 but in a 4″ × 4″ FOV and without contours for the ^{12}CO moment-zero map. In some ^{18}CO maps, we draw a dashed circle centered on the continuum source, 0.″5 in radius, for reference.

3000–5000 au could infall toward the star (see Section 5.1 for further discussion).

The southern part of the envelope (D, D′) is brighter than the northern part in Figures 3 and 6, i.e., at both large (up to $\sim 10^4$ au) and small ($\lesssim$3000 au) spatial scales. A similar asymmetry at the $\gg$1000 au scales of the envelope CO emission has previously been observed for a few other FUors and FUor-like stars by Fehér et al. (2017), Kóspál et al. (2017b), and Ruíz-Rodríguez et al. (2017b). The C^{18}O emission in Figure 6 shows peaks at the southeast and northwest at 13.7 and 14.1 km s^{-1}, offset by ∼0.″5 (∼800 au), without exhibiting an emission peak at the continuum position. This contrasts with the envelopes of Class 0–I YSOs, whose envelope emission peaks at the star (e.g., Arce & Sargent 2006). One would estimate a dynamical scale of these components of $\sim 1 \times 10^5$ yr with the given distance from the continuum source and the offset velocity (∼0.2 km s^{-1}). Therefore, such an asymmetry in the innermost envelope would disappear within a fairly short timescale compared with the entire timescale of the envelope dissipation, i.e., the termination of the Class I phase ($(4–5) \times 10^5$ yr; see Dunham et al. 2014, for a review). This fact suggests that this asymmetry in the innermost region is associated with an activity or phenomenon significantly shorter than the above dynamical timescale (see Section 4.3).

4.3. Interaction with a Hot FUor Wind?

Reipurth et al. (2012) observed P Cygni profiles in optical permitted lines (Hα, Na D, Ca II) toward the star. These line profiles indicate the presence of a hot ($\gg$1000 K) energetic wind ($v \sim 200$ km s^{-1}), as for many other FUors (Hartmann & Kenyon 1996; Audard et al. 2014). How is this FUor wind interacting with the extended molecular outflows and the envelope seen in the CO emission?

As reported by Thommes et al. (2011) and Reipurth et al. (2012), the outburst began between 1953 and 2009. If we assume that the wind seen in the optical line profiles emerged at the onset of the outburst, we would expect that in 65 yr, the wind would have traveled ∼2700 au (∼2″). However, none of the CO lines exhibit clear evidence of the interaction between the wind and the surrounding material within this 2″ window.

In contrast, within ∼0.″5 (∼800 au) of the continuum emission, the ^{12}CO line at the base of the redshifted outflow (B′) shows the presence of bright high-velocity emission up to ∼19 km s^{-1} (Figures 5 and 7). Furthermore, the ^{18}CO emission in Figure 6 is relatively faint within ∼0.″5 compared with the outer region. These may be due to interaction with the hot FUor wind, i.e., high-velocity ^{12}CO emission due to acceleration by the FUor wind and a deficit of C^{18}O due to a cavity opened by the FUor wind.

In summary, interactions between the hot FUor wind and the circumstellar environment are limited to within 0.″5 (corresponding to ∼800 au) of the star at worst. The FUor wind has emerged relatively recently, considering the fact that a wind with $v \sim 200$ km s^{-1} would require only ∼20 yr to reach this distance. This fact suggests that the FUor outburst associated with this star has begun relatively recently, i.e., closer to 2009 than 1953, as constrained by the time range provided by optical imaging observations by Thommes et al. (2011) and Reipurth et al. (2012).

4.4. Continuum and Circumstellar Disk

We measured a size of the compact dust continuum emission at the star of $100^{+35}_{-24} \times 87^{+32}_{-22}$ au (Section 3.1). With the measured flux of 9.0 ± 0.9 mJy, we derive a typical temperature of the disk of 60–120 K, assuming an optically thick disk with a uniform temperature. The inferred temperature is higher if the filling factor of the area is less than the unity due to a low optical thickness or gravitational fragmentation of the disk (Section 1). In Table 4, we compare the observed flux and angular scale for V900 Mon with ALMA

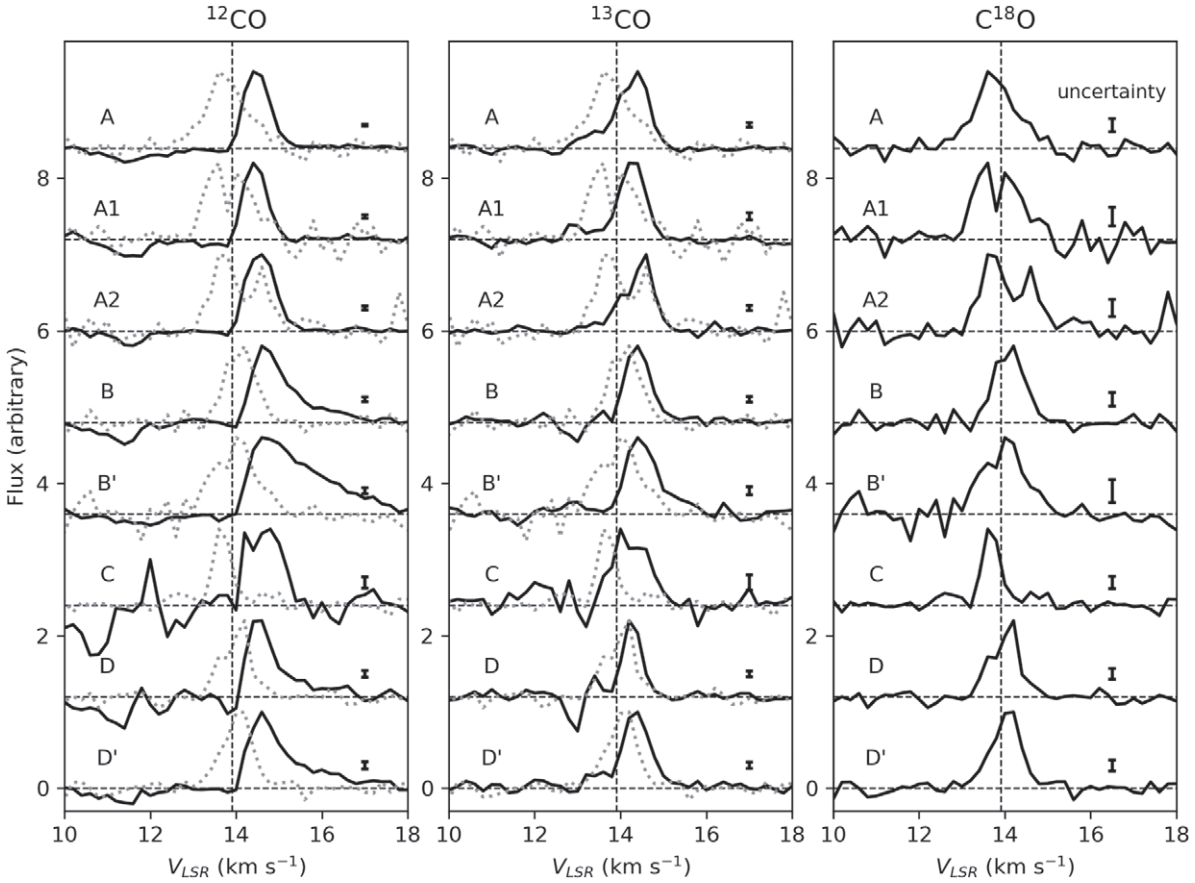

Figure 7. The ^{12}CO, ^{13}CO, and C^{18}O line profiles extracted for the individual features discussed in the text. Each line profile is normalized to the peak and arbitrarily offset. The uncertainty of each profile is shown on the right. For ^{12}CO and ^{13}CO, we overplot the C^{18}O profiles at the same position with gray dotted curves for comparison. The vertical dashed line shows the reference velocity (13.9 km s^{-1}; see text).

Table 3
Peak and FWHM Velocities for C^{18}O Emission

Feature/Area[a]	V_{peak} (km s^{-1})	V_{FWHM} (km s^{-1})
A	13.6	0.9
A1	13.6/14.0	1.2
A2	13.6–13.8/14.6	1.3
B	14.2	0.8
B′	14.0–14.2	1.1
C	13.6–13.8	0.5
D	14.2	0.8
D′	14.0–14.2	0.8
N2	13.6	0.2
N1	13.6–13.8	0.6
S1	14.0–14.2	0.9
S2	14.2	0.3

Note.
[a] See Sections 3 and 4.1 for the definition of A–D′ and N1/N2/S1/S2, respectively.

observations of several other FUor and FUor-like stars at the same wavelength (Kóspál et al. 2017a; Cieza et al. 2018). The table shows that these parameters for V900 Mon are similar to those for other FUors, except for the large spatial scale observed for V346 Nor.

Compact millimeter continuum emission associated with FUors is often attributed to a circumstellar disk (e.g., Kóspál et al. 2017a; Cieza et al. 2018; Liu et al. 2018). All of the targets in Table 2 except V346 Nor would infer a disk radius below 100 au. To further investigate the nature of the millimeter emission, Cieza et al. (2018) conducted radiative transfer modeling of passive disks, for which the heating source of the disk is radiation from the central star. These authors used a small radius for the disk (20–40 au) to reproduce their millimeter observations.

In contrast, Liu et al. (2016) and Takami et al. (2018) conducted near-IR observations of scattered light in five well-studied FUors. Some of these objects show that scattered light, presumably associated with a disk surface, extends over 400–800 au, i.e., significantly larger than the radii of the millimeter continuum emission described above. Therefore, the compact nature of the millimeter disk emission would require the following physical processes.

(A) Viscous disk accretion in the inner disk region—This physical process, which is not included in the models by Cieza et al. (2018), heats up the FUor disk, in particular in the inner region, and enhances the radiation from the inner disk (see Hartmann & Kenyon 1996, for a review). As a result, the observed FWHM size of the entire emission region will be smaller. In the Appendix we provide simple calculations to demonstrate the compact nature of the millimeter emission. This physical process would simultaneously explain a typical temperature of >60–120 K (see above), which is significantly higher than that assumed for circumstellar disks associated with Class II YSOs heated by stellar radiation at an ∼100 au scale (∼20 K; Williams & Cieza 2011).

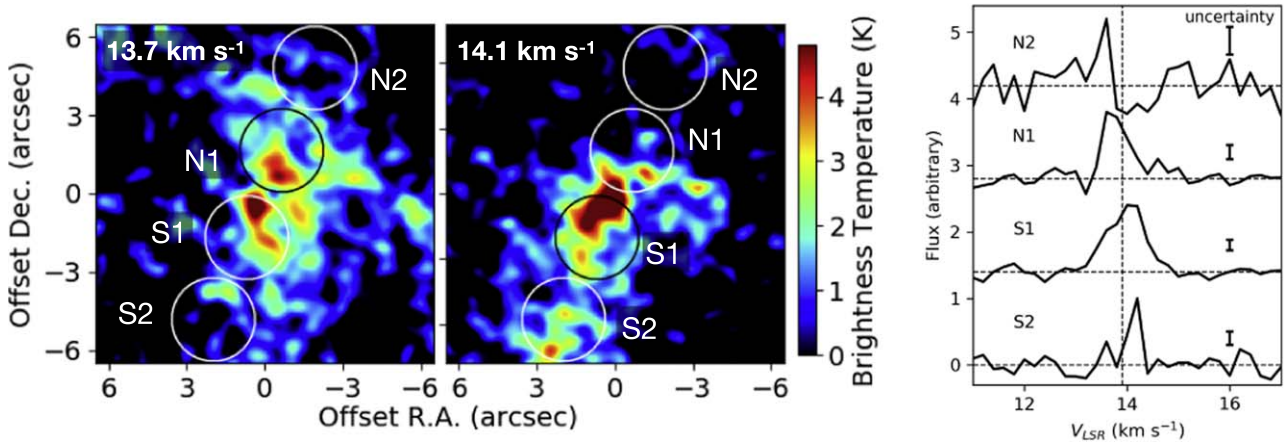

Figure 8. (Left) Areas for extracting line profiles, plotting over the velocity channel maps of the $C^{18}O$ emission. (Right) Line profiles.

Table 4
ALMA Observations of the 1.3 mm Continuum Associated with FUor Disks

Object	Category	L_{bol} ($L_\odot$)	d (kpc)	Onset (yr)	$F_{1.3\ mm}$ (mJy)		FWHM[c] (au)	Resolution[d] (au)	References
					Measured	$d = 1$ kpc[b]			
V900 Mon	FUor	∼200[a]	1.5	1953–2010	9.0 ± 0.9	20 ± 2	$100^{+35}_{-24} \times 87^{+32}_{-22}$	600 × 450	This work
V346 Nor	FUor	135	0.7	∼1980	27 ± 3	13 ± 1	420 × 322	770 × 630	Kóspál et al. (2017a)
V883 Ori	FUor-like	400	0.41	⋯	353 ± 35	59 ± 7	$124^{+9}_{-9} \times 100^{+8}_{-8}$	103 × 70	Cieza et al. (2018)
HBC 494	FUor-like	300	0.41	⋯	113 ± 11	20 ± 2	$58^{+5}_{-5} \times 19^{+5}_{-5}$	103 × 70	Cieza et al. (2018)
V2775 Ori	FUor/EXor	∼25	0.41	2005–2007	106 ± 10	18 ± 2	$61^{+4}_{-4} \times 59^{+5}_{-5}$	103 × 70	Cieza et al. (2018)

Notes.
[a] We scale the luminosity measured by Reipurth et al. (2012) to the recent measurement of the distance based on *Gaia* DR2 (Section 1).
[b] Scaled to the given distance. The uncertainty of the distance is not included.
[c] Measured by fitting the continuum emission and the beam using two-dimensional Gaussians in the image plane.
[d] Spatial resolution of the observations. The uncertainty of the distance is not included.

(B) Gravitational instability in the outer disk region—This physical process could be responsible for triggering the FUor outbursts (Section 1) and would fragment the outer disk region as shown by numerical simulations (e.g., Vorobyov & Basu 2015; Zhao et al. 2018). This would decrease the surface density in the bulk of the outer disk by forming compact, dense, and very optically thick clumps. As a result, this would decrease the millimeter continuum emission from the outer radii (>100 au), but a small fraction of leftover dust (of an order of $\sim 10^{-6}\ M_\odot$) would allow near-IR scattered light to be observed at these radii, as shown by Liu et al. (2016) and Takami et al. (2018).

(C) Grain growth and their inward drift—Numerical simulations by Vorobyov et al. (2018a) demonstrated that grain growth in the circumstellar disk can occur in the early stage of protostellar evolution ($t \sim 0.1$ Myr), during which FUor outbursts can occur (Section 5). While small dust grains ($a < 1\ \mu$m) can be dynamically coupled with the gas content of the disk, large grains ($a > 1\ \mu$m) can lose angular momentum via friction with the gas component of the disk and therefore gradually drift toward the star. Vorobyov et al. (2018a) demonstrated that, due to these physical processes, the fraction of millimeter-to-micron-sized grains can be larger in the inner radii, in particular within ∼100 au of the star. This may be observed in millimeter emission as its compact intensity distribution, as millimeter-sized grains have an opacity significantly larger than that of micron-sized grains (e.g., Wood et al. 2002; Dong et al. 2012).

Among the above three physical processes, only (A) could simultaneously explain the warm and compact nature of the millimeter dust emission. Even so, processes (B) and/or (C) may also contribute to its compact nature.

If we attribute the continuum emission to the disk only, the observed spatial scale implies a disk inclination of up to 48° from face-on. One may speculate that the disk has a larger inclination angle, close to edge-on, because of (1) the CO intensity distribution of the extended outflow and the elongated envelope (Sections 3.2, 3.3, and 4.2) and (2) a relatively larger extinction despite a relatively low envelope mass (Section 1). This would require some contribution from a wind or wind cavity to the observed flux. The intense radiation from the inner disk would illuminate and heat the wind cavity close to the star, making thermal emission contribute to the observed flux. While the FUors are associated with a hot energetic ionized wind, as shown using optical spectroscopy (e.g., Hartmann & Kenyon 1996; Reipurth et al. 2012), it would not be likely that free–free emission from a wind or jet significantly contributes to the observed flux and therefore its angular scale. Liu et al. (2017) executed a detailed analysis of millimeter and centimeter emission for FU Ori and showed that free–free continuum emission from the ionized jet or wind is <0.1 mJy at 230 GHz.

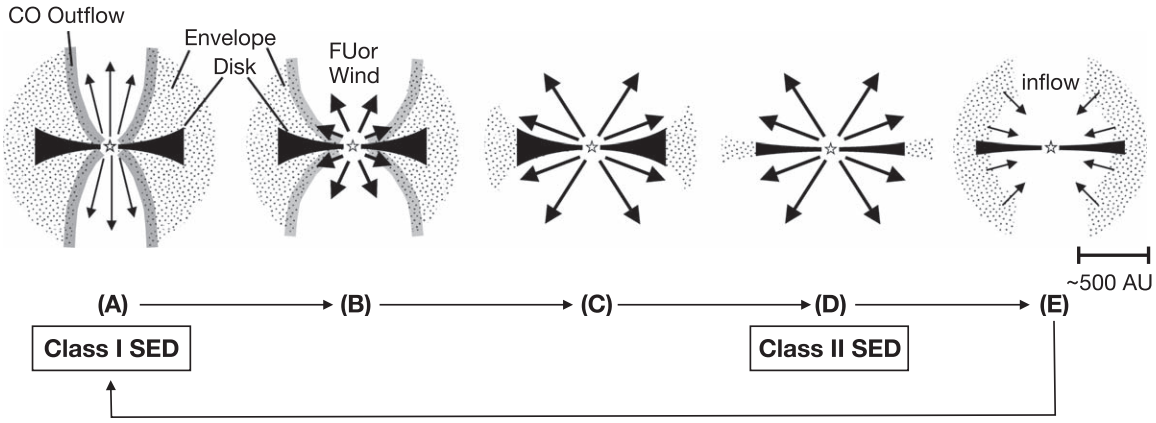

Figure 9. Proposed sequence of the wind and infall associated with FUor outbursts. The arrows indicate the motion of gas flow due to a jet, wind, or infall. Adapted from Takami et al. (2018).

The emission would be significantly fainter for V900 Mon, which has a distance about three times farther than FU Ori.

5. Toward a Unified Scheme for Low-mass Protostellar Evolution

The key issues for FUor outbursts are (1) their triggering mechanism and (2) whether most normal YSOs experience such accretion outbursts during their evolution (Section 1). A variety of circumstellar structures seen in near-IR scattered light suggest gravitational instabilities in disks as a triggering mechanism of the outbursts (Dong et al. 2016; Liu et al. 2016; Takami et al. 2018). A combination of hydrodynamical simulations and radiative transfer calculations supports this mechanism, as well as the scenario that many YSOs experience similar accretion outbursts (Dunham & Vorobyov 2012; Dong et al. 2016). In this section, we extend our discussion for the latter issue.

The evolutionary stages of normal low-mass YSOs are characterized by their IR SEDs (Class 0→ I→II→III; Stahler & Palla 2005). Some authors apply this SED classification for normal YSOs to FUors (e.g., Green et al. 2013; Gramajo et al. 2014). However, the SEDs of FUors during the outbursts may not indicate their evolutionary stages. This is because the repetition of the following processes would change the SED (Class I↔ II) on a significantly shorter timescale than low-mass protostellar evolution: (1) an energetic FUor wind blowing away the circumstellar material responsible for a large mid-to-far-IR excess and (2) gas+dust infall from the outer to the inner envelope, recovering the circumstellar dust+gas responsible for the mid-to-far-IR excess. We discuss this issue in detail in Section 5.1.

In Sections 5.2 and 5.3 we compare observations of several FUors and FUor-like objects and the envelope mass and collimation of the extended CO outflow observed for a limited sample of normal Class 0–II YSOs. Arce & Sargent (2006) observed the CO outflows and envelopes associated with Class 0, I, and II YSOs using millimeter interferometry. These authors showed that the envelope mass becomes smaller and the opening angle of the CO outflow becomes larger during the Class 0→ I→II evolution. In Section 5.2 we discuss the cases of V900 Mon and V346 Nor, for which the associated CO outflows and envelopes are similar to normal Class 0–I YSOs. These support the idea that most normal YSOs experience FUor outbursts during their evolution. In Section 5.3 we discuss the cases for a few FUor-like objects (V883 Ori, HBC 494, V2775 Ori) for which the extended CO outflows may be widened by hot energetic FUor winds.

5.1. Possible Time Variation of IR SEDs

Liu et al. (2016) and Takami et al. (2018) executed near-IR imaging polarimetry of five classical FUors to observe scattered light in their circumstellar environment. Their polarized intensity distributions show a variety of morphologies with arms, tails or streams, spikes, and fragmented distributions among the objects. The morphologies of these reflection nebulae differ significantly from those of many other normal YSOs. The authors attributed these structures to gravitationally unstable disks, trails of clump ejections, dust blown by a wind or jet, and a stellar companion.

Why do the FUors we observed look very different from each other in the near-IR? Takami et al. (2018) proposed that YSOs follow the sequence summarized in Figure 9 with accretion outbursts and associated winds. A normal Class I YSO before the outburst is associated with a circumstellar disk, a circumstellar envelope, and an extended CO outflow (A in the figure). The circumstellar envelope exists below the wall of the outflow cavity. The disk cannot be seen in the near-IR because it is embedded in an optically very thick circumstellar envelope. When an episodic energetic FUor wind emerges with the FUor outburst, it blows away the surface of the circumstellar disk and the inner region of the envelope at ∼1000 au (B–D in the figure). As a result, a variety of structures associated with the disk become visible in the near-IR, as for normal Class II YSOs. When the FUor wind stops, circumstellar material from the outer region infalls, quickly reassembling the disk and inner envelope (E in the figure). The freefall timescale is only ∼5000 yr at 1000 au for a 1 $M_{\odot}$ central star. These processes would repeat during the Class I evolutionary phase (i.e., a timescale of (4–5) × 10^5 yr; see Dunham et al. 2014, for a review) and gradually clear the outer envelope (i.e., that observable using a single-dish millimeter telescope or in mid-IR silicate absorption; see, e.g., Sandell & Weintraub 2001; Green et al. 2006; Quanz et al. 2007; Kóspál et al. 2017b) toward the Class II evolutionary phase discussed for normal YSOs (Kóspál et al. 2017b).

Given a typical luminosity of ∼200 $L_{\odot}$ for FUors, the mid-to-far-IR SEDs would originate from the inner envelope or the outer disk ($r \lesssim$ 1000 au) heated by radiation from the inner disk

(Zhu et al. 2008) or the central star (Elbakyan et al. 2019). Johnstone et al. (2013) demonstrated that the thermal budget with radiation cooling quickly reaches equilibrium with a timescale of light-crossing time (i.e., ∼6 days for 1000 au). Therefore, the above processes would change the IR SED on a timescale significantly shorter than the Class I evolutionary phase.

5.2. Implications of the Envelope and Extended CO Outflows: V900 Mon and V346 Nor

Similar to many other YSOs, V900 Mon is associated with cold gas ($T < 50$ K) in an extended molecular bipolar outflow and an envelope. Its spatial scale in our ALMA observations is at least $\sim 10^4$ au (Sections 3 and 4). Interaction with a hot energetic wind ($\Delta v \sim 200\,\mathrm{km\,s^{-1}}$), presumably associated with the FUor outburst, is limited to the region only up to ∼800 au (Section 4.3). Therefore, the intensity distribution for most parts of the extended CO outflow and envelope has presumably remained the same since the pre-outburst phase, and we would be able to discuss the nature of the progenitor of this FUor. For V900 Mon, the envelope mass in the literature (0.027 $M_\odot$; Gramajo et al. 2014) and the CO outflow opening angle shown by our observations (∼70° and ∼120° at $r \sim 5000$ au for the blueshifted and redshifted lobes, respectively) are similar to Class I YSOs (e.g., 0.03–0.05 $M_\odot$ and 70°–160° at $r \sim 5000$ au; Arce & Sargent 2006), suggesting that the progenitor of this FUor is a normal Class I YSO.

The millimeter observations of V346 Nor also show an envelope mass and extended CO outflow collimation similar to a normal YSO. Kóspál et al. (2017a) observed the CO outflows, envelope, and disk associated with this object using ALMA, in which the bipolar outflow extends over an $\sim 10^4$ au scale. Its envelope mass (0.3–1 $M_\odot$; Evans et al. 1994; Sandell & Weintraub 2001; Kóspál et al. 2017b) and the outflow collimation are similar to Class 0 YSOs rather than Class I YSOs, as shown by Arce & Sargent (2006).

As with V900 Mon, V346 Nor does not show clear evidence for interaction between the hot FUor wind and the extended CO outflow and envelope. This star went into eruption some time between 1976 and 1980, showed a rapid fading in 2010–2011, then brightened again (see Kóspál et al. 2017a, for a summary). If the energetic wind emerged at the onset of the outburst in 1976–1980, the wind would reach up to ∼5000 au, adopting a velocity similar to that of the other FUors (up to $\sim 600\,\mathrm{km\,s^{-1}}$; Audard et al. 2014). However, the CO observations made by Kóspál et al. (2017a) do not show discontinuous intensity distributions between the inside and outside of this radii up to $\sim 10^4$ scales. Therefore, we assume that we can discuss the progenitor based on the associated envelope and extended CO outflows.

5.3. Cases of V883 Ori, HBC 494, and V2775 Ori

These FUor-like objects are associated with an envelope with 0.1–0.4 $M_\odot$ (Sandell & Weintraub 2001; Caratti o Garatti et al. 2011; Gramajo et al. 2014; Kóspál et al. 2017b), comparable to those of Class 0 YSOs (∼0.2 $M_\odot$; Arce & Sargent 2006). However, the morphologies of their CO outflows observed using ALMA differ significantly from those of Class 0 protostars. Ruíz-Rodríguez et al. (2017a, 2017b) showed that the outflows associated with HBC 494 and V883 Ori have opening angles significantly larger than those of Class 0 YSOs, similar to Class II YSOs observed by Arce & Sargent (2006). Zurlo et al. (2017) showed that the star is associated with a pair of blueshifted and redshifted rings or shells in the CO emission that can be explained by a bipolar outflow but are not usually observed toward normal Class 0–II YSOs.

The outflow morphologies inconsistent with the Class 0 phase (i.e., those suggested by the envelope mass) can be explained if their outflows are due to interactions between the ambient gas and a hot energetic FUor wind, as suggested by Ruíz-Rodríguez et al. (2017a) for V883 Ori. However, Zurlo et al. (2017) pointed out that the latest outbursts associated with V2775 Ori cannot explain the observed CO outflow at 4000–8000 au, considering the dates of observations and a typical outflow velocity. In this context, the CO outflows associated with V2775 Ori may have been driven by winds associated with the previous outbursts.

Why would we see interaction with the FUor winds associated with the previous outbursts for V2775 Ori but not V900 Mon or V346 Nor? The time intervals between the FUor outbursts and the associated winds may span a wide range of scales for different stars, and even for the same stars. Vorobyov & Basu (2015) and Vorobyov et al. (2018b) executed numerical hydrodynamics simulations with gravitationally unstable disks and reproduced outbursts with time intervals of $30–10^5$ yr. According to their simulations, compact infalling fragments trigger isolated outbursts with time intervals between the outbursts of >1000 yr if the tidal torques do not disintegrate the fragments. If a fragment starts disintegrating when it is migrating to the inner disk, it will cause a cluster of outbursts with time intervals of <1000 yr. In these contexts, the time intervals of FUor outbursts associated with individual objects would highly depend on the disk conditions and hence on the initial conditions in their parental prestellar cores and their evolutionary status.

6. Conclusions

We observed ^{12}CO, ^{13}CO, and C^{18}O $J = 2$–1 lines and the 230 GHz continuum for the FUor V900 Mon ($d \sim 1.5$ kpc) using ALMA with a $0\farcs2 \times 0\farcs15$ resolution. The ^{12}CO maps show the presence of an extended molecular bipolar outflow in the east–west direction at an $\sim 10^4$ au scale. The ^{13}CO maps show compressed gas at the cavity wall. The C^{18}O maps show the presence of a rotating envelope across the jet axis extending over an $\sim 10^4$ au scale.

Previous optical spectroscopy shows the presence of a hot energetic FUor wind at the star, with $v \sim 200\,\mathrm{km\,s^{-1}}$. This wind may be responsible for high-velocity (Δv up to $\sim 5\,\mathrm{km\,s^{-1}}$) ^{12}CO emission and a possible cavity in the C^{18}O emission within $0\farcs5$ (∼800 au) of the star. We do not have any clear evidence for this wind interacting with molecular gas at larger distances. This suggests that most parts of the extended CO outflows and the envelope are the same as before the onset of the outburst.

The envelope mass and CO outflow collimation of V900 Mon suggest that the progenitor of this FUor is a normal Class I YSO. Similarly, the progenitor of another FUor, V436 Nor, may be a normal Class 0 YSO. These results are consistent with the idea that FUor outbursts occur for most YSOs. In contrast, extended CO outflows associated with some FUor-like stars (V883 Ori, HBC 494, V2775 Ori) may be driven or widened by a hot energetic wind that is often observed toward FUors.

As with other FUor and FUor-like stars, V900 Mon is associated with compact continuum millimeter emission. We measured an FWHM angular scale of 0.″06 (~90 au) using a two-dimensional Gaussian fitting for the millimeter emission and the beam, respectively. The emission is associated with a dusty circumstellar disk, plus possible emission from a wind or wind cavity near the base. The temperature of the region seems to be significantly higher than usually assumed for a disk associated with normal YSOs.

The observed spatial scale of the probable disk emission is significantly smaller than that of the disks associated with some FUors and that seen in the near-IR. The warm and compact nature of the disk continuum emission could be explained with viscous heating of the disk, although gravitational fragmentation in the outer disk and/or a combination of grain growth and their inward drift may also contribute to its compact nature.

This project has received funding from the European Research Council (ERC) under the European Union's Horizon 2020 research and innovation program under grant agreement No. 716155 (SACCRED). M.T. and T.S.C. are supported by the Ministry of Science and Technology (MoST) of Taiwan (grant No. 106-2119-M-001-026-MY3). M.T. and H.B.L. are supported by MoST of Taiwan 108-2923-M-001-006-MY3 for the Taiwanese-Russian collaboration project. E.I.V. acknowledges support from the Russian Foundation for Basic Research (RFBR), Russian-Taiwanese project No. 19-52-52011. This paper makes use of the following ALMA data: ADS/JAO. ALMA #2016.1.00209.S and #2017.1.00451.S. ALMA is a partnership of the ESO (representing its member states), NSF (USA), and NINS (Japan), together with the NRC (Canada), MoST and ASIAA (Taiwan), and KASI (Republic of Korea), in cooperation with the Republic of Chile. The Joint ALMA Observatory is operated by the ESO, AUI/NRAO, and NAOJ. This work has made use of data from the European Space Agency (ESA) mission *Gaia* (https://www.cosmos.esa.int/gaia), processed by the *Gaia* Data Processing and Analysis Consortium (DPAC; https://www.cosmos.esa.int/web/gaia/dpac/consortium). Funding for the DPAC has been provided by national institutions, in particular the institutions participating in the *Gaia* Multilateral Agreement. This research made use of the Simbad database operated at CDS, Strasbourg, France, and NASA's Astrophysics Data System Abstract Service.

Facility: ALMA.

Software: CASA (McMullin et al. 2007), numpy (Oliphant 2006), scipy (Jones et al. 2001).

Appendix
Millimeter Continuum Emission from a Viscous Disk

We use a simple conventional flat-disk model, used extensively for FUors over many years (e.g., Calvet et al. 1991a; Zhu et al. 2007, 2008), to demonstrate the compact nature of the observed millimeter emission. According to this model, the accretion luminosity from the disk and the temperature distribution are described as follows (e.g., Zhu et al. 2007):

$$L_{\rm acc} = \frac{GM_*\dot{M}}{2R_i}, \tag{1}$$

$$T_{\rm eff}^4(r) = \frac{3GM_*\dot{M}}{8\pi\sigma r^3}\left[1 - \left(\frac{R_i}{r}\right)^{1/2}\right], \tag{2}$$

Table 5
Model Parameters

Initial Parameters		
Accretion luminosity from the disk ($L_{\rm acc}$)	100 $L_\odot$[a]	
Frequency (ν)	230 GHz	
Total flux (F_ν)	9.0 mJy	
Dust opacity ($\kappa_{\rm ext}$)	0.2 $\rm m^2\ kg^{-1}$[b]	
Inner disk radius (R_i)	5 $R_\odot$[c]	
Outer disk radius ($r_{\rm out}$)	300 au	
Distance	1500 pc	
Sublimation temperature $T_{\rm sub}$	1500 K[d]	
Derived Parameters	$i = 0°$	$i = 60°$
Dust surface density Σ at $r = 1$ au ($\rm kg\ m^{-2}$)	1.0×10^2	1.4×10^2
Sublimation radius $r_{\rm sub}$ (au)	0.29	0.29
Radius for $\tau = 1$ (au)	20.3	55.8
Total dust mass ($M_\odot$)	2.2×10^{-3}	3.0×10^{-3}

Notes.
[a] See text.
[b] Beckwith et al. (1990).
[c] Zhu et al. (2007), Gramajo et al. (2014).
[d] Lodders (2003).

where $L_{\rm acc}$ is the accretion luminosity, G is the gravitational constant, M_* is the stellar mass, $\dot{M}$ is the mass accretion rate, R_i is the disk inner radius (=the stellar radius), $T_{\rm eff}(r)$ is the effective temperature at the disk radius r, and σ is the Stefan–Boltzmann constant. From these equations, we derive

$$T_{\rm eff}(r) = \left\{\frac{3R_iL_{\rm acc}}{4\pi\sigma r^3}\left[1 - \left(\frac{R_i}{r}\right)^{1/2}\right]\right\}^{1/4}. \tag{3}$$

Equation (3) indicates that we can calculate the temperature distribution with the given disk radius, inner disk radius, and accretion luminosity from the disk without measuring/assuming the stellar mass and/or mass accretion rate.

The intensity from each part of the disk would be described as

$$I_\nu(r) = B_\nu(r)(1 - e^{-\tau(r)}), \tag{4}$$

$$B_\nu(r) = \frac{2h\nu^3}{c^2}\frac{1}{\exp[\frac{h\nu}{kT_{\rm eff}(r)}] - 1}, \tag{5}$$

where $I(r)$ is the intensity, $B(r)$ is the blackbody radiation, h is the Planck constant, ν is the frequency of the observations, c is light speed, and k is the Boltzmann constant. The parameter $\tau(r)$ is the optical thickness, which is described as $\kappa_{\rm ext}\Sigma(r)(\cos i)^{-1}$, where $\kappa_{\rm ext}$ is the dust opacity, $\Sigma(r)$ is the dust surface density, and i is the disk inclination angle. Here we adopt $\Sigma(r) \propto r^{-1}$ based on previous observations of disks for Class II YSOs (e.g., Williams & Cieza 2011; Takami et al. 2013). Therefore,

$$\tau(r) = \kappa_{\rm ext}\Sigma_0 r^{-1}(\cos i)^{-1}. \tag{6}$$

We discuss submillimeter emission from the dust continuum; therefore, we assume

$$\tau(r) = 0 \quad \text{for } T > T_{\rm sub}, \tag{7}$$

where $T_{\rm sub}$ is the sublimation temperature of the dust grains. We note that if the maximum temperature in the disk is above

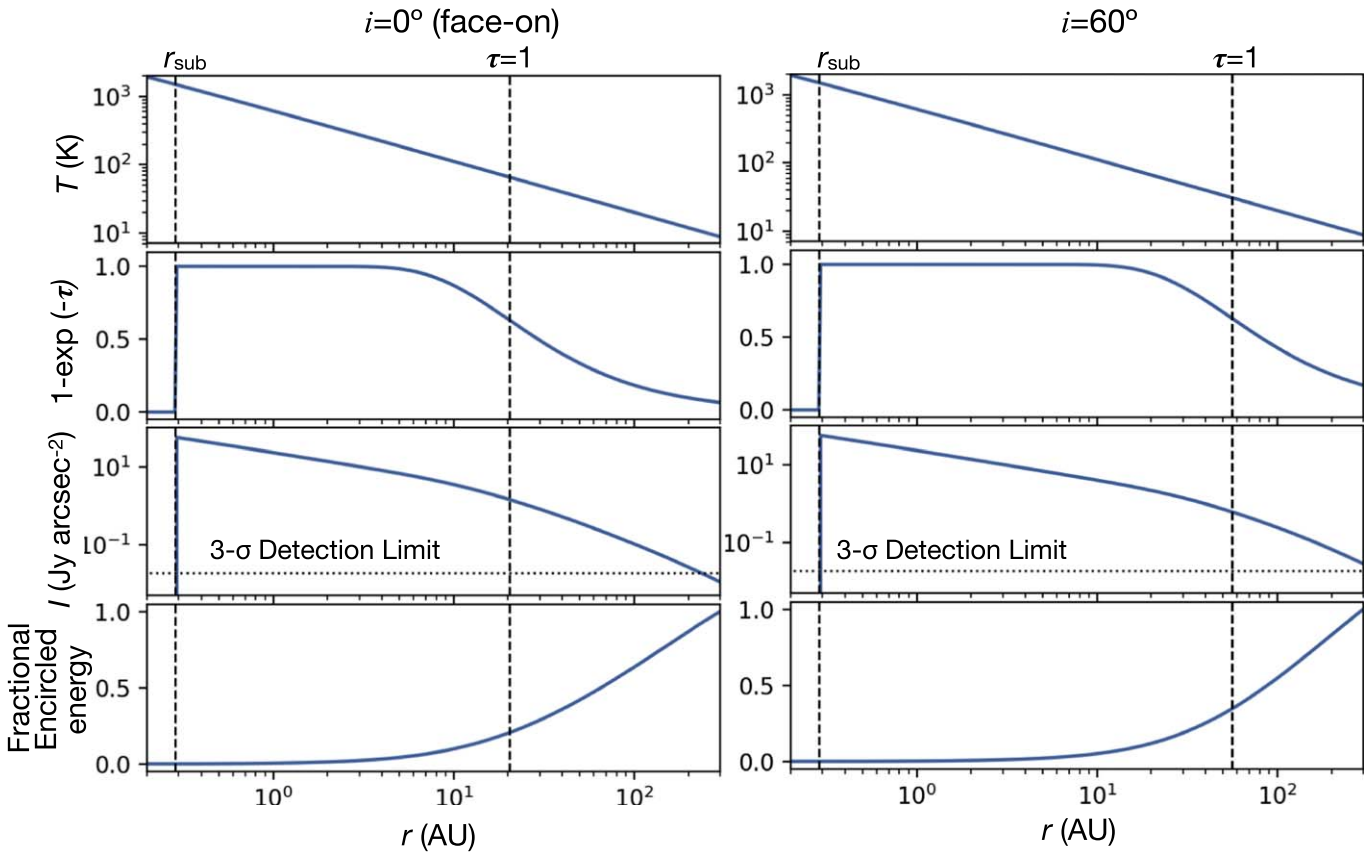

Figure 10. Physical parameters of the viscous disk model (see text for details). The left and right panels are for disk inclination angles of 0° (face-on view) and 60°, respectively. The vertical dashed lines show the dust sublimation radius and the radius for optical thickness $\tau = 1$. The horizontal dotted line in the third box shows the detection limit of our ALMA observations.

$T_{\rm sub}$, Equations (2) and (3) provide two radii for the sublimation temperature, one comparable to the stellar radius R_i and the other significantly larger. This is because Equations (2) and (3) provide the maximum temperature $T_{\rm max}$ at $r = 1.36\ R_i$, and the temperature monotonically decreases inward and outward, respectively (Zhu et al. 2007). However, Zhu et al. (2007) pointed out that these equations provide an unphysical temperature distribution at $r < 1.36\ R_i$. Therefore, we only use the outer sublimation radius (hereafter $r_{\rm sub}$) and assume $I_\nu(r) = 0$ and $\tau(r) = 0$ for $r < r_{\rm sub}$.

The spatially integrated flux is described as

$$F_\nu = \int_{R_i}^{r_{\rm out}} \frac{2\pi r I(r)\cos i}{d^2} dr = \frac{2\pi \cos i}{d^2} \int_{r_{\rm sub}}^{r_{\rm out}} r I(r) dr, \quad (8)$$

where $r_{\rm out}$ is the outer radius of the disk and d is the distance to the target. In this equation, we replace the inner disk radius R_i with the sublimation radius $r_{\rm sub}$ because the latter should be significantly larger than the former. This is corroborated by the fact that the FUors are associated with optical and near-IR emission from the inner disk with a spectral type of K-M or earlier, indicating that the temperature of the inner disk region exceeds $T \gtrsim 3000$ K (Hartmann & Kenyon 1996; Audard et al. 2014).

We can calculate the flux F_ν using Equations (3)–(8) as a function of the accretion luminosity from the disk $L_{\rm acc}$, frequency of the observations ν, dust opacity $\kappa_{\rm ext}$, constant to scale the surface density Σ_0, disk inclination angle i, inner radius R_i, outer radius $r_{\rm out}$, and distance d. With the given $L_{\rm acc}$, ν, $\kappa_{\rm ext}$, i, R_i, $r_{\rm out}$, and d, the flux F_ν is a function of Σ_0 only. We adjusted Σ_0 to match the flux to the observations using `scipy.interpolate.interp1d`.

The upper part of Table 5 summarizes the parameters we used for the simulations. We tentatively set the disk accretion luminosity $L_{\rm acc}$, a dust opacity $\kappa_{\rm ext}$, and the outer disk radius $r_{\rm out}$ as follows.

1. $L_{\rm acc}$—We assume 100 $L_\odot$, about half of the observed bolometric luminosity ($\sim$200 $L_\odot$; Section 1 and Table 4), for the following reason. The primary energy sources of the observed bolometric luminosity would be accretion heating in the disk (see, e.g., Hartmann & Kenyon 1996, for a review) and at the central star (Baraffe et al. 2012; Elbakyan et al. 2019). The fraction of these disk/stellar accretion luminosities is uncertain and time-variable (Elbakyan et al. 2019). Fortunately, our calculations depend on the assumed accretion luminosity only marginally, as seen in Equation (3).
2. $\kappa_{\rm ext}$—We assume 0.2 $\rm m^2\ kg^{-1}$ following Beckwith et al. (1990). This value is also time-variable with grain growth (Vorobyov et al. 2018a). A larger fraction of millimeter-sized grains would provide a lower dust opacity (e.g., Dong et al. 2012) and therefore a large surface density and total disk mass based on Equation (7).
3. $r_{\rm out}$—We assume 300 au, i.e., comparable to the area where we measure the flux and FWHM of the continuum emission. In reality, the disk emission may extend beyond this radius below the detection limit (Figure 10).

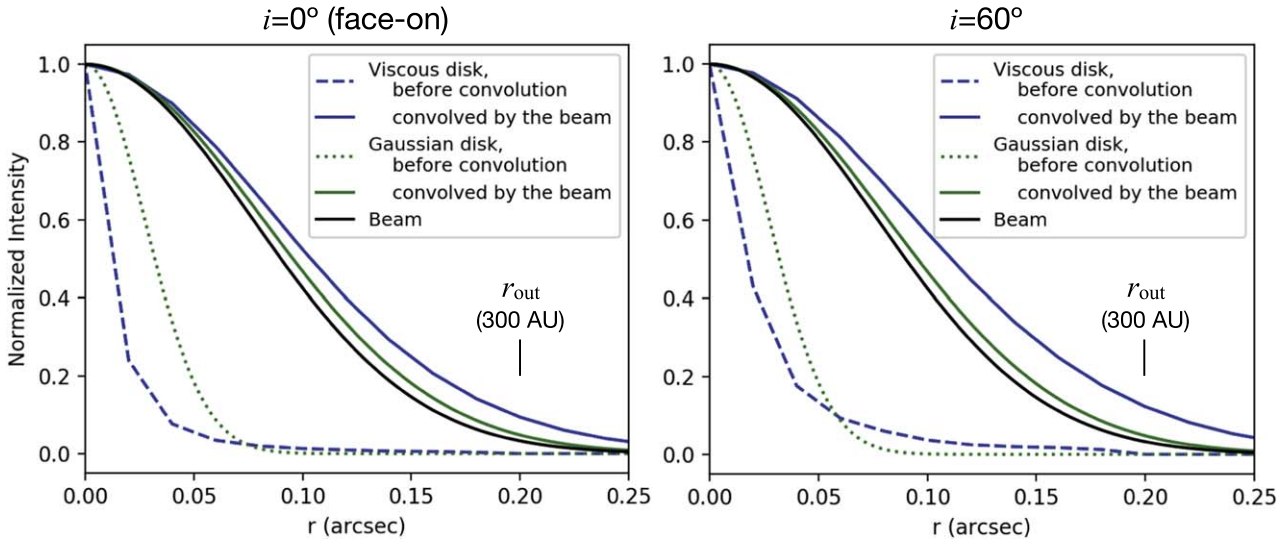

Figure 11. Spatial distribution of the viscous and Gaussian disk models and their pseudo-observations with a Gaussian with an FWHM = 0.″18 beam. The left and right panels are for disk inclination angles of 0° (face-on view) and 60°, respectively. We use a 0.″02 pixel sampling (i.e., the same as the observed data) for the original and convolved distributions of the viscous disk models.

Figure 10 and the lower part of Table 5 show the modeled results for disk inclination angles of 0° (face-on view) and 60°. To compare the intensity distribution with the observations, we conducted monochromatic Monte Carlo simulations using the intensity distribution in Figure 10 and convolved with the pseudo-beam of the observations, i.e., a two-dimensional Gaussian with an FWHM of 0.″18. Similarly, we convolved the "Gaussian disk" used in Section 3.1 (0.″064 FWHM) using the same beam to represent our ALMA observations in that section. Their profiles are shown in Figure 11. We used 10^5 photons to obtain the image of the viscous disk at each disk inclination angle.

As shown in Figure 11, the viscous disk models provide intensity distributions highly concentrated at the center. In contrast, the outer disk region (like $r > 50$–100 au) contributes to the total flux as significantly as the inner disk (Figure 10) and therefore to the observed intensity distribution after the convolution. In Figure 11, both the viscous and Gaussian disk models show marginal extension beyond the beam of the observations, but the former is slightly larger than the latter. The viscous disk models yield an FWHM of the observations of 0.″21 and 0.″22, respectively. These are 9% and 16% larger than that with the Gaussian disk model, i.e., that represents the ALMA observations in Section 3.1.

More realistic models, which are beyond the scope of this paper, require the following treatments: (1) vertical temperature gradients in the disk (e.g., Calvet et al. 1991a, 1991b; Vorobyov et al. 2014); (2) scattering of the millimeter radiation in the disk, which would degrade the emission from the inner disk region (e.g., Liu 2019); (3) illumination of the outer disk by the inner disk or the central star (e.g., Zhu et al. 2007; Dong et al. 2016; Liu et al. 2016; Cieza et al. 2018); and (4) low Planck opacities in the outer disk, which may make Equation (2) invalid.

ORCID iDs

Michihiro Takami https://orcid.org/0000-0001-9248-7546
Hauyu Baobab Liu https://orcid.org/0000-0003-2300-2626
Ágnes Kóspál https://orcid.org/0000-0001-7157-6275
Péter Ábrahám https://orcid.org/0000-0001-6015-646X
Eduard I. Vorobyov https://orcid.org/0000-0002-6045-0359
Fernando Cruz-Sáenz de Miera https://orcid.org/0000-0002-4283-2185
Timea Csengeri https://orcid.org/0000-0002-6018-1371
Joel Green https://orcid.org/0000-0003-1665-5709
Michiel Hogerheijde https://orcid.org/0000-0001-5217-537X
Tien-Hao Hsieh https://orcid.org/0000-0002-5507-5697
Ruobing Dong https://orcid.org/0000-0001-9290-7846
Alfonso Trejo https://orcid.org/0000-0001-8365-6563

References

Arce, H. G., & Sargent, A. I. 2006, ApJ, 646, 1070
Arce, H. G., Shepherd, D., Gueth, F., et al. 2007, in Protostars and Planets V, ed. B. Reipurth et al. (Tucson, AZ: Univ. Arizona Press), 245
Audard, M., Ábrahám, P., Dunham, M. M., et al. 2014, in Protostars and Planets VI, ed. H. Beuther et al. (Tucson, AZ: Univ. Arizona Press), 387
Baraffe, I., Vorobyov, E., & Chabrier, G. 2012, ApJ, 756, 118
Beckwith, S. V. W., Sargent, A. I., Chini, R. S., & Guesten, R. 1990, AJ, 99, 924
Calvet, N., Hartmann, L., & Kenyon, S. J. 1991a, ApJ, 383, 752
Calvet, N., Hartmann, L., & Strom, S. E. 2000, in Protostars and Planets IV, ed. V. Mannings, A. P. Boss, & S. S. Russell (Tucson, AZ: Univ. Arizona Press), 377
Calvet, N., Patino, A., Magris, G. C., & D'Alessio, P. 1991b, ApJ, 380, 617
Caratti o Garatti, A., Garcia Lopez, R., Scholz, A., et al. 2011, A&A, 526, L1
Cieza, L. A., Casassus, S., Tobin, J., et al. 2016, Natur, 535, 258
Cieza, L. A., Ruíz-Rodríguez, D., Perez, S., et al. 2018, MNRAS, 474, 4347
Connelley, M. S., & Greene, T. P. 2010, AJ, 140, 1214
Connelley, M. S., & Reipurth, B. 2018, ApJ, 861, 145
Cruz-Sáenz de Miera, F., Kóspál, Á., Ábrahám, P., Liu, H. B., & Takami, M. 2019, ApJL, 882, L4
Dong, R., Hashimoto, J., Rafikov, R., et al. 2012, ApJ, 760, 111
Dong, R., Vorobyov, E., Pavlyuchenkov, Y., Chiang, E., & Liu, H. B. 2016, ApJ, 823, 141
Doppmann, G. W., Greene, T. P., Covey, K. R., & Lada, C. J. 2005, AJ, 130, 1145
Dunham, M. M., Stutz, A. M., Allen, L. E., et al. 2014, in Protostars and Planets VI, ed. H. Beuther et al. (Tucson, AZ: Univ. Arizona Press), 195
Dunham, M. M., & Vorobyov, E. I. 2012, ApJ, 747, 52
Elbakyan, V. G., Vorobyov, E. I., Rab, C., et al. 2019, MNRAS, 484, 146
Evans, N. J., II, Balkum, S., Levreault, R. M., Hartmann, L., & Kenyon, S. 1994, ApJ, 424, 793
Fehér, O., Kóspál, Á., Ábrahám, P., Hogerheijde, M. R., & Brinch, C. 2017, A&A, 607, A39

Gaia Collaboration, Brown, A. G. A., Vallenari, A., et al. 2018, A&A, 616, A1
Gramajo, L. V., Rodón, J. A., & Gómez, M. 2014, AJ, 147, 140
Green, J. D., Evans, N. J., II, Kóspál, Á., et al. 2013, ApJ, 772, 117
Green, J. D., Hartmann, L., Calvet, N., et al. 2006, ApJ, 648, 1099
Greene, T. P., & Lada, C. J. 1996, AJ, 112, 2184
Hales, A. S., Corder, S. A., Dent, W. R. D, et al. 2015, ApJ, 812, 134
Hartmann, L., & Kenyon, S. J. 1996, ARA&A, 34, 207
Johnstone, D., Hendricks, B., Herczeg, G. J., & Bruderer, S. 2013, ApJ, 765, 133
Jones, E., Oliphant, T., Peterson, P., et al. 2001, SciPy: Open Source Scientific Tools for Python, http://scipy.org
Kenyon, S. J., Hartmann, L. W., Strom, K. M., & Strom, S. E. 1990, AJ, 99, 869
Kóspál, Á., Ábrahám, P., Csengeri, T., et al. 2017a, ApJ, 843, 45
Kóspál, Á., Ábrahám, P., Csengeri, T., et al. 2017b, ApJ, 836, 226
Lee, C., Mundy, L. G., Stone, J. M., & Ostriker, E. C. 2002, ApJ, 576, 294
Liu, H. B., Dunham, M. M., Pascucci, I., et al. 2018, A&A, 612, A54
Liu, H. B., Takami, M., Kudo, T., et al. 2016, SciA, 2, e1500875
Liu, H. B., Vorobyov, E. I., Dong, R., et al. 2017, A&A, 602, A19
Liu, H. B. 2019, ApJL, 877, L22
Lodders, K. 2003, ApJ, 591, 1220
Lucas, P. W., & Roche, P. F. 1996, MNRAS, 280, 1219
Lucas, P. W., & Roche, P. F. 1998, MNRAS, 299, 699
Mathis, J. S. 2000, in Circumstellar and Interstellar Material, ed. A. N. Cox (4th ed.; New York: AIP Press, Springe), 523
McMullin, J. P., Waters, B., Schiebel, D., Young, W., & Golap, K. 2007, in ASP Conf. Ser. 376, Astronomical Data Analysis Software and Systems XVI, ed. R. A. Shaw, F. Hill, & D. J Bell (San Francisco, CA: ASP), 127
Muzerolle, J., Hartmann, L., & Calvet, N. 1998, AJ, 116, 2965
Oliphant, T. E. 2006, A Guide to NumPy, https://ieeexplore.ieee.org/document/4160250
Padgett, D. L., Brandner, W., Stapelfeldt, K. R., et al. 1999, AJ, 117, 1490
Quanz, S. P., Henning, T., Bouwman, J., et al. 2007, ApJ, 668, 359
Reipurth, B., Aspin, C., & Herbig, G. H. 2012, ApJL, 748, L5
Ruíz-Rodríguez, D., Cieza, L. A., Williams, J. P., et al. 2017a, MNRAS, 468, 3266
Ruíz-Rodríguez, D., Cieza, L. A., Williams, J. P., et al. 2017b, MNRAS, 466, 3519
Sandell, G., & Weintraub, D. A. 2001, ApJS, 134, 115
Stahler, S. W., & Palla, F. 2005, The Formation of Stars (Weinheim: Wiley-VCH)
Takami, M., Fu, G., Liu, H. B., et al. 2018, ApJ, 864, 20
Takami, M., Karr, J. L., Hashimoto, J., et al. 2013, ApJ, 772, 145
Tamura, M., Gatley, I., Joyce, R. R., et al. 1991, ApJ, 378, 611
Thommes, J., Reipurth, B., Aspin, C., & Herbig, G. H. 2011, CBET, 2795
Varricatt, W. P., Kerr, T. H., Carroll, T., & Moore, E. 2015, ATel, 8174
Vorobyov, E., Akimkin, V., Stoyanovskaya, O., Pavlyuchenkov, Y., & Liu, H. B. 2018a, A&A, 614, 98
Vorobyov, E. I., & Basu, S. 2015, ApJ, 805, 115
Vorobyov, E. I., Elbakyan, V. G., Plunkett, A. L., et al. 2018b, A&A, 613, A18
Vorobyov, E. I., Pavlyuchenkov, Y. N., & Trinkl, P. 2014, ARep, 58, 522
Williams, J. P., & Cieza, L. A. 2011, ARA&A, 49, 67
Wood, K., Wolff, M. J., Bjorkman, J. E., & Whitney, B. 2002, ApJ, 564, 887
Zhao, B., Caselli, P., Li, Z.-Y., & Krasnopolsky, R. 2018, MNRAS, 473, 4868
Zhu, Z., Hartmann, L., Calvet, N., et al. 2007, ApJ, 669, 483
Zhu, Z., Hartmann, L., Calvet, N., et al. 2008, ApJ, 684, 1281
Zurlo, A., Cieza, L. A., Williams, J. P., et al. 2017, MNRAS, 465, 834